Master's Thesis

Numerical Simulations for Ground Motion Amplifications on the Gentle Hill during the 2017 M_L5.4 Pohang Earthquake

Junyoung Lee

Department of Urban and Environmental Engineering
(Urban Infrastructure Engineering)

Graduate School of UNIST

2020

Numerical Simulations for Ground Motion Amplifications at the Gentle Hill during the 2017 M_L5.4 Pohang Earthquake

Junyoung Lee

Department of Urban and Environmental Engineering
(Urban Infrastructure Engineering)

Graduate School of UNIST

Numerical Simulations for Ground Motion Amplifications at the Gentle Hill during the 2017 M_L5.4 Pohang Earthquake

Numerical Simulations for Ground Motion Amplifications at the Gentle Hill during the 2017 M_L5.4 Pohang Earthquake
submitted to the Graduate School of UNIST
in partial fulfillment of the
requirements for the degree of
Master of Science

Junyoung Lee

01/07/2020
Approved by

_____

Advisor
Byungmin Kim

Numerical Simulations for Ground Motion Amplifications at the Gentle Hill during the 2017 M_L5.4 Pohang Earthquake

Junyoung Lee

This certifies that the thesis/dissertation of Junyoung Lee is approved.

01/07/2020

signature

_____

Advisor: Byungmin Kim

signature

_____

Thesis Committee Member: Young-Joo Lee

signature

_____

Thesis Committee Member: Seokho Jeong

Abstract

The November, 15, 2017, Pohang, South Korea, earthquake with a local magnitude (M_L) of 5.4 caused diverse damage to buildings near the epicenter. This study focuses on the correlation between ground motion amplifications by topographic effects and damage pattern at the town of Gokgang-ri. Severe damage such as cracks and collapses occurred in a northern part of the town located on slopes, plateaus, or ridges facing the epicenter, whereas only minor damage occurred to buildings located on the opposite side of the slope. Northern part and southern part of the town have similar geological and soil condition. Two aftershocks were recorded at temporary seismic stations. A series of numerical simulations were conducted using the recorded ground motions and soil properties were measured in Gokgang-ri. It turned out that there are large ground motion amplifications at the slopes and ridges facing the epicenter. The ground motion amplificationss are influenced by incidence angle. In this study, amplifications for input motions with incidence angles of 10° and 15° are relatively lager than those for input motions with 0° and 20°.

Table of Contents

LIST OF FIGURES

LIST OF TABLES

1. Introduction

The Pohang earthquake (M_L5.4) occurred on November, 15, 2017 and it inflicted several degrees of damage to buildings on the gentle hills near an epicenter. The pattern of damages on buildings shows that it was concerned with topography. Surface wave is amplified or attenuated by the topography irregularity. Ashford and Sitar (1997) reported that waves propagating into the slope are amplified at the crest of the slope and waves propagating away from the slope are attenuated. There are numerous example about topographic amplifications. During 1994 Northridge earthquake (**M**6.7), The peak acceleration at a ridge on Pacoima Canyon, Los Angeles, California recorded ~1.6 g which is about three times larger than those at a bottom of Pacoima Canyon (Sepúlveda et al., 2005) and such observations were found in Davis and West (1973), Pedersen et al. (1994), Stewart and Sholtis (2005), and Buech et al. (2010). During the Pohang earthquake, topographic amplification may have occurred on a topographic relief (such as a hill, a slope, a ridge, etc.) near the epicenter. Kang et al. (2019b) analyzed the phenomenon using a site investigations (i.e. Multichannel analysis of surface waves and downhole test) and ground motions recorded at temporary stations. The first part of this study presents an overview of the Pohang earthquake, study area (i.e. Gokgang-ri), damage pattern, and recorded motion at temporary station. Subsequently, it presents a series of numerical simulations for the gentle hills near the epicenter.

2. Pohang earthquake and study area

2.1. 2017 M5.4 Pohang, South Korea, Earthquake

Pohang suffered from diverse range of damages by an earthquake (M_L5.4) occurred on the November, 15, 2017 which is recorded as the second-largest in the history of instrumental earthquake for Korea. the earthquake is located at 36.11°N, 129.37°E with a focal depth of ~4.5km (Kim et al., 2018). Kim et al. (2018) also reported that it is possible that hydraulic stimulation at Pohang enhanced geothermal system site near the epicenter of mainshock induced the earthquake.

There are numerous faults in Korea as shown in Figure 1 (a) (National Emergency Management Agency, 2012). The Pohang city are surrounded by major fault of YangSan Fault, Yonil Tectonic Line, UlSan Fault, and Ochen Fault as shown in Figure 1(b) (Son et al., 2005).

The Korea Meteorological Administration (KMA) and Korea Institute of Geoscience and Mineral Resources (KIGAM) reported information of the mainshock and the four major aftershocks with magnitudes of greater than 3 that occurred until 20 November 2017 and Table 1 (Korea Meteorological Administration, 2017) summarized it. Main shock's focal depth on 15 November 2017 was estimated to be 3–7 km (Kim et al. (2018) reported that a focal depth of the mainshock is ~4.5 km).

The fault type of the mainshock was considered as an oblique, reverse and fault with dextral strike-slip. It featured a northeast strike, a length of 6.3 km in the direction of the strike, a width of up

to 3.4 km, and a dip of approximately 60–70°. The fault type of aftershock with M4.3 was considered as a reverse fault with NNE direction strike and a focal depth of 6 km. The type of faults of the other three aftershocks were considered as strike-slip faults with focal depths in a range of 2–3 km.

Two foreshocks (M2.2 and M2.6) were generated approximately 7 minutes before the main shock and 100 aftershocks over the magnitude of 2.0 occurred by May, 31, 2018 (Korea Meteorological Administration, 2018).

Table 1. Fault information for the mainshock and the four major aftershocks with a magnitude of greater than 3 that occurred until 20 November (reference from the Korea Meteorological Administration (2017))

Earthquake	Occurrence data (local time)	Magnitude (M)	Focal depth (km)	Focal mechanism	Fault type
Main shock	15 November 14:29:31	5.4	3-7 (~4.5)	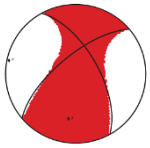	Oblique (reverse and dextral strike-slip) (strike: NE)
Aftershocks	15 November 16:49:30	4.3	6	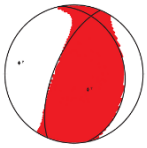	Reverse (strike: NNE)
	16 November 09:02:42	3.6	2	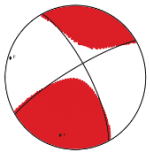	Strike-slip
	19 November 23:45:31	3.5	3	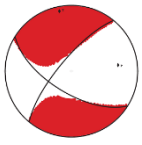	
	20 November 14:29:31	3.6	3	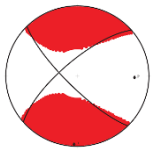	

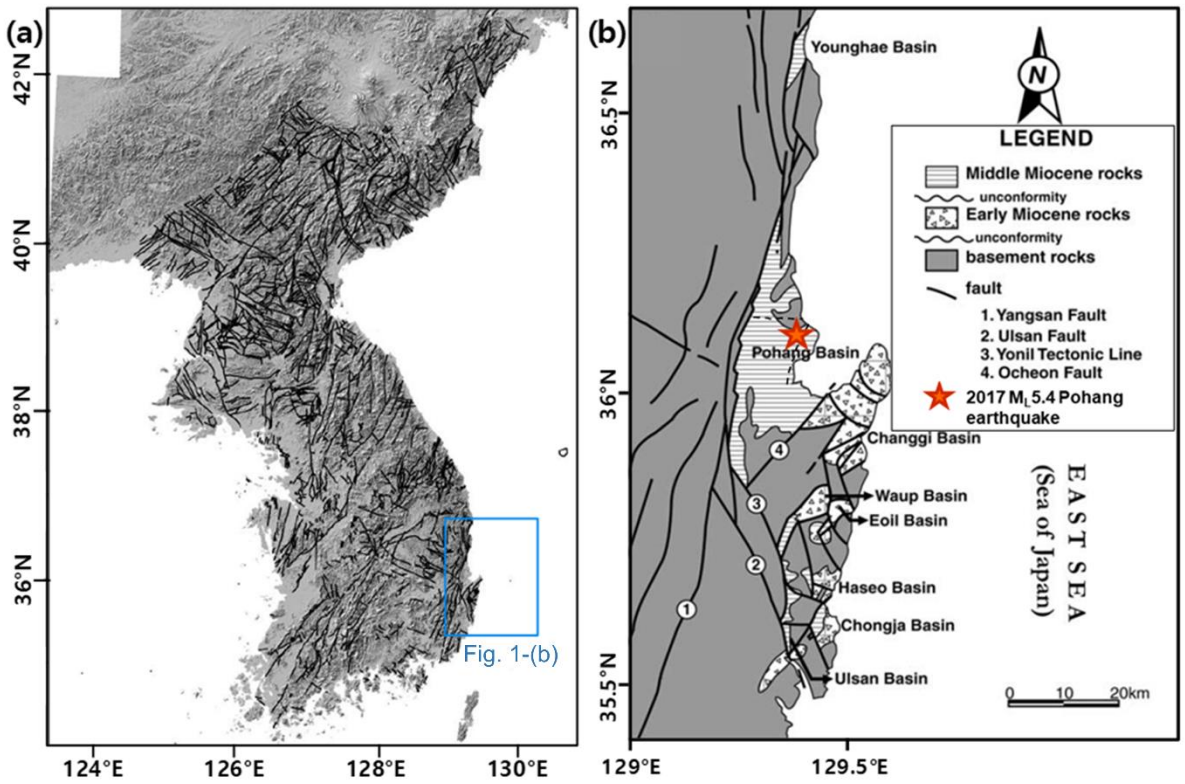

Figure 1. (a) Fault map of the South Korea (National Emergency Management Agency, 2012) and (b) major and small faults near the Pohang city (Son et al., 2005) edited by Kang et al. (2019a)

2.2. Study area and damage pattern

The study area of Gokgang-ri located around 3.5 km to the east of the main shock epicenter, as shown in Figure 2, is a small town with 65 households. Most of the buildings are single story built before the 1980s; approximately 39% are wooden structures and 44% masonry structures, and both types lack earthquake resistance. The others (17%) are reinforced concrete structures.

The type of damage affected on all 65 houses in the town was investigated using a visual inspection. the damage was classified into five damage grades based on criteria established in Kang et al. (2019b): (1) damage grade 1: no damage observed; (2) damage grade 2: small crack with width narrower than 5 mm; (3) damage grade 3: moderate crack with width exceeding 5 mm; (4) damage grade 4: quite serious damage to structural components such as columns and/or ground deformation, ground cracks, and lateral spreading; (5) damage grade 5: completely demolished or abandoned houses as shown in Figure 3. Of the 65 houses in the study area, 12, 16, 21, 11, and 5 houses (∼18:5%, 24.6%, 32.3%, 16.9%, and 7.7%, respectively) were classified into damage grades from 1 to 5, respectively, as shown in Figure 4a.

Northern district of Gokgang-ri had severe damage such as building collapse, on the other hand

southern district had only minor damage, as shown in Figure 4a. Both districts are at a similar distance from the main shock and aftershocks and Same geologic formation. Therefore, the difference of damage patterns between northern district and southern district couldn't be explained by these factors.

The two districts are located on gentle slopes that have different aspects. The northern district is located on the slopes facing the epicenter, on plateaus, or on ridges, whereas the southern district located on slopes facing the opposite direction. Therefore, the difference in the damage pattern may have been concerned with the different topographies.

To prove the hypothesis, Kang et al. (2019b) recorded aftershocks at three temporary seismic stations in Gokgang-ri immediately. The locations of the three stations are shown in Figure 4a. The coordinates of the three temporary stations (i.e., GOK1, GOK2, and GOK4) are 36.1090° N and 129.4069° E, 36.1063° N and 129.4051° E, and 36.1090° N and 129.4090° E, respectively.

The two topographic profiles in Figure 4b (i.e., Line-1 and Line-2) in a west–east direction show the two blue lines in Figure 4a where the temporary seismic stations are installed. The main shock, and two aftershocks, propagated from the west of Gokgang-ri as assumed in Figure 4b.

Kang et al. (2019b) conducted Downhole tests at BH-1 and BH-2 near the GOK1 and GOK2, respectively, to measure shear velocity profiles (V_S) as shown in Figure 5. At depths greater than 8 m, V_S profiles at these two sites are similar, where the V_S range from 350 to 420 m/s. At depths shallower than 8 m, BH-1 has the V_S profile varying from 320 to 340 m/s, whereas BH-2 has it ranging from 240 to 280 m/s. They also conducted MASW at GOK1, GOK2, and GOK4 also to measure shear velocity profiles. The VS profiles obtained from the MASW conducted near GOK1 and GOK2 correspond with those from the downhole tests at BH-1 and BH-2, respectively as shown in Figure 5.

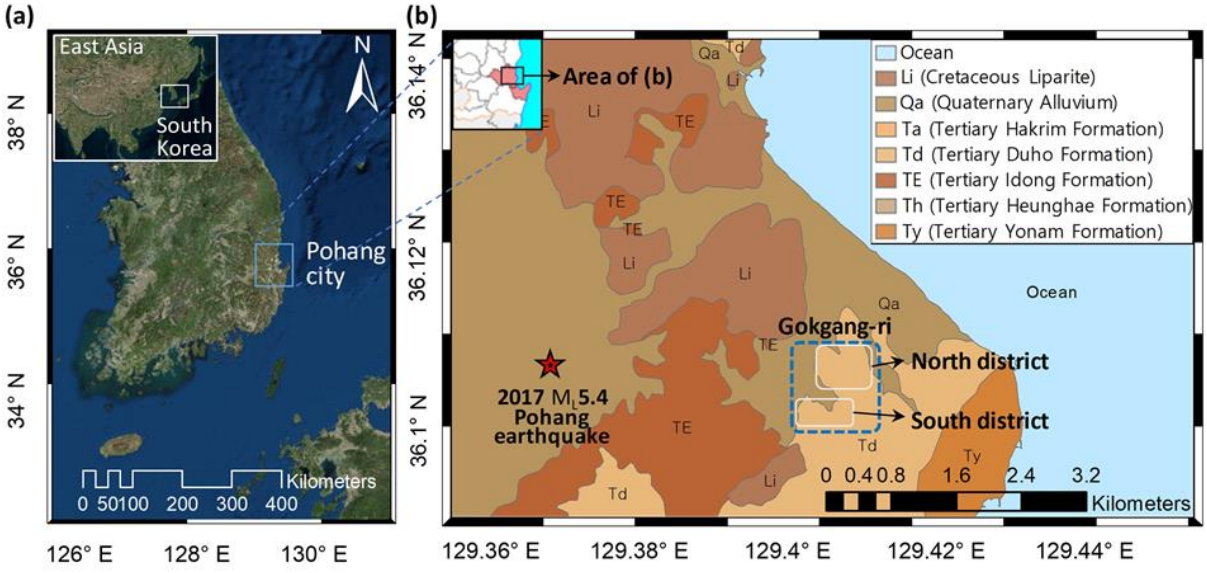

Figure 2. (a) Map of South Korea, (b) Geological map of study area Gokgang-ri (Geological survey of Korea, 1964) (Kang et al., 2019b)

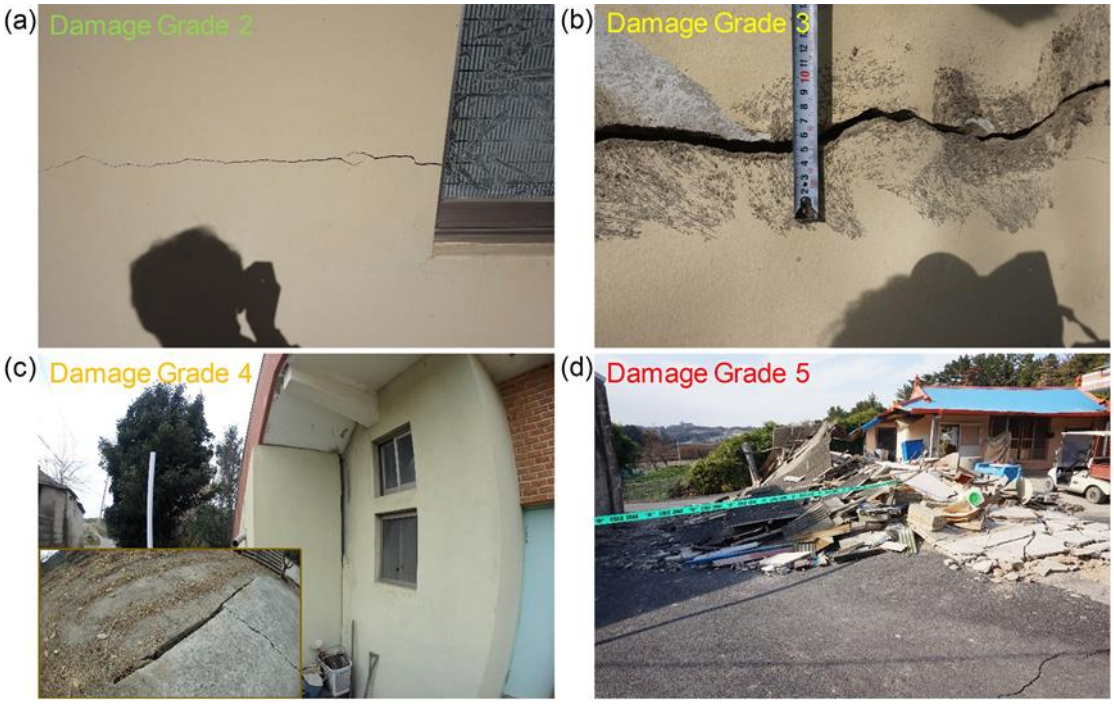

Figure 3. Example of damage grades 2-5 (Kang et al., 2019b).

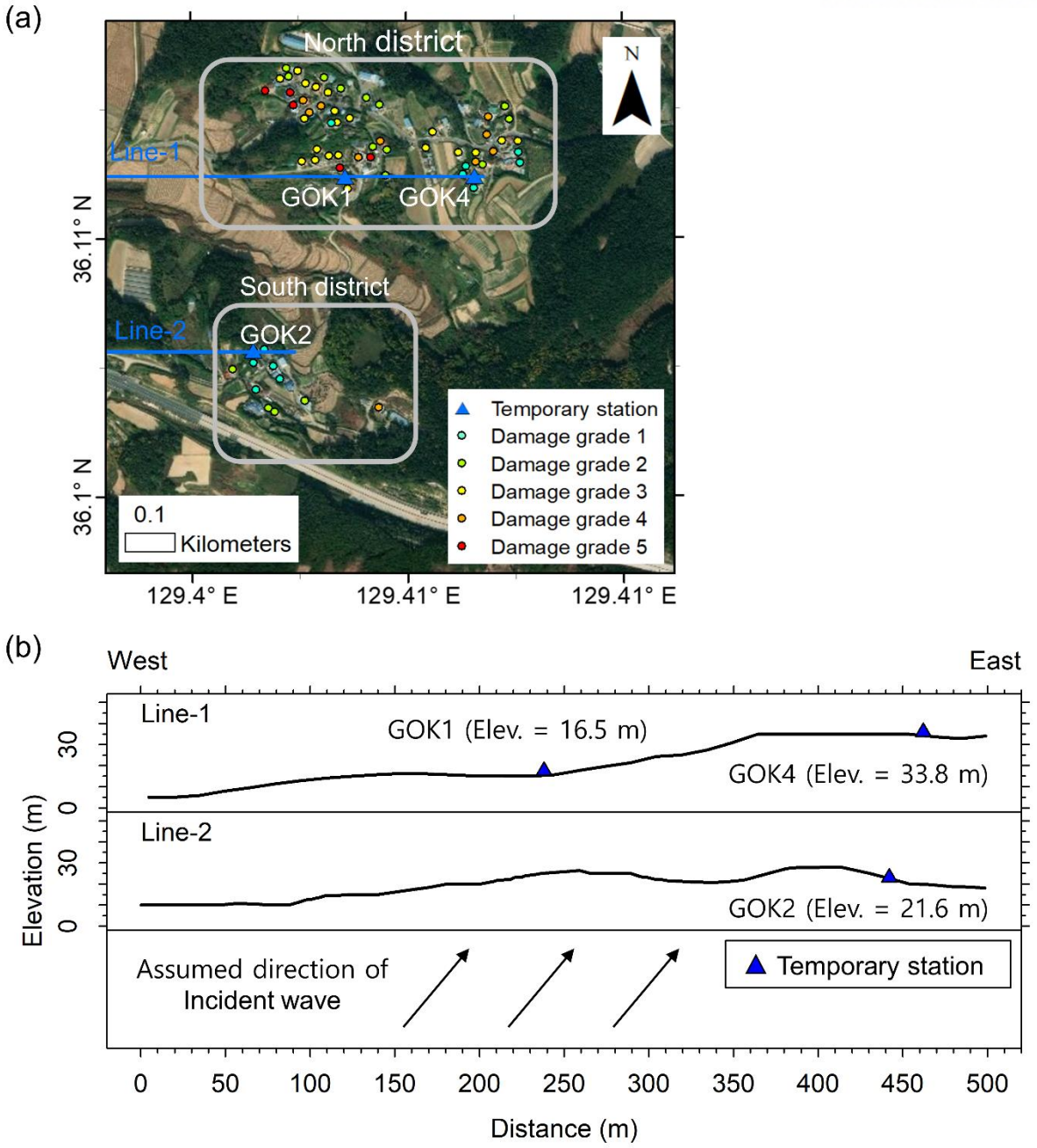

Figure 4. (a) Gokgang-ri damage pattern and location of temporary seismic station (GOK1, GOK2, and GOK4) (b) topographic profiles in a west–east direction according to the three blue lines shown in (a). Epicenter of main shock was about 3.5 km to the west.

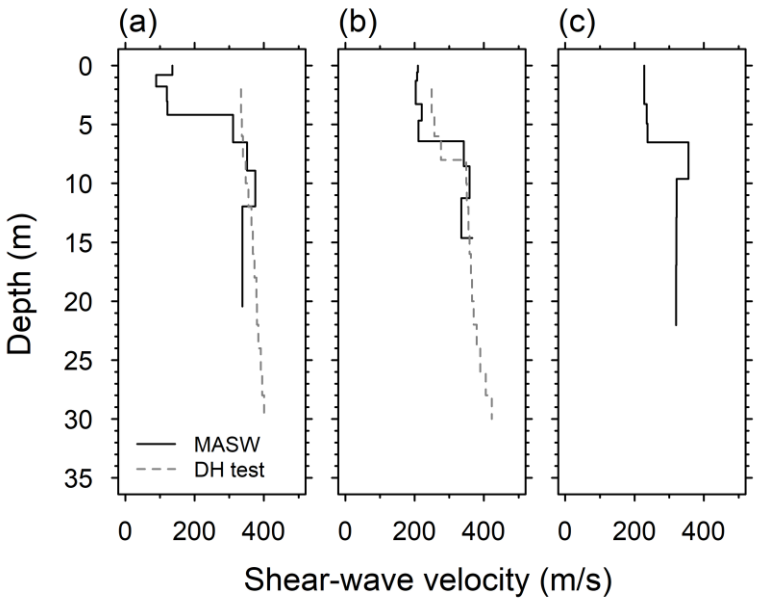

Figure 5. Shear-wave velocity profile near GOK1, GOK2 and GOK4 measured by multichannel analysis of surface wave (MASW) method and downhole (DH) test near GOK1 and GOK2.

3. Aftershock ground motion records

Figure 6 shows epicenters of the main shock, two aftershocks (AS 1 and AS 2), and three temporary seismic stations (GOK1, GOK2, and GOK4). AS 1 (M_L 3.5) and AS 2 (M_L 2.8) were recorded on 25 December 2017 and 27 December 2017, respectively at a rate of 200Hz. AS 1 and AS 2 are ~4.5km away from the study area and focal depths are 7.9 and 9.5 km, respectively. The measured acceleration time series of the two aftershocks in east-west (EW), north-south (NS), and up-down (UD) direction at the three temporary stations are shown in Figure 7 (a) and (b), respectively. Peak ground acceleration (PGAs) of the measured acceleration at GOK2 are smaller than those at GOK1 and GOK2 in all direction. Calculated 5% damped spectral acceleration of two aftershocks are shown in Figure 8 (a) and (b), respectively. The Sas at period of 0.01-0.2s of GOK1 and GOK4 are larger than those of GOK2 overall.

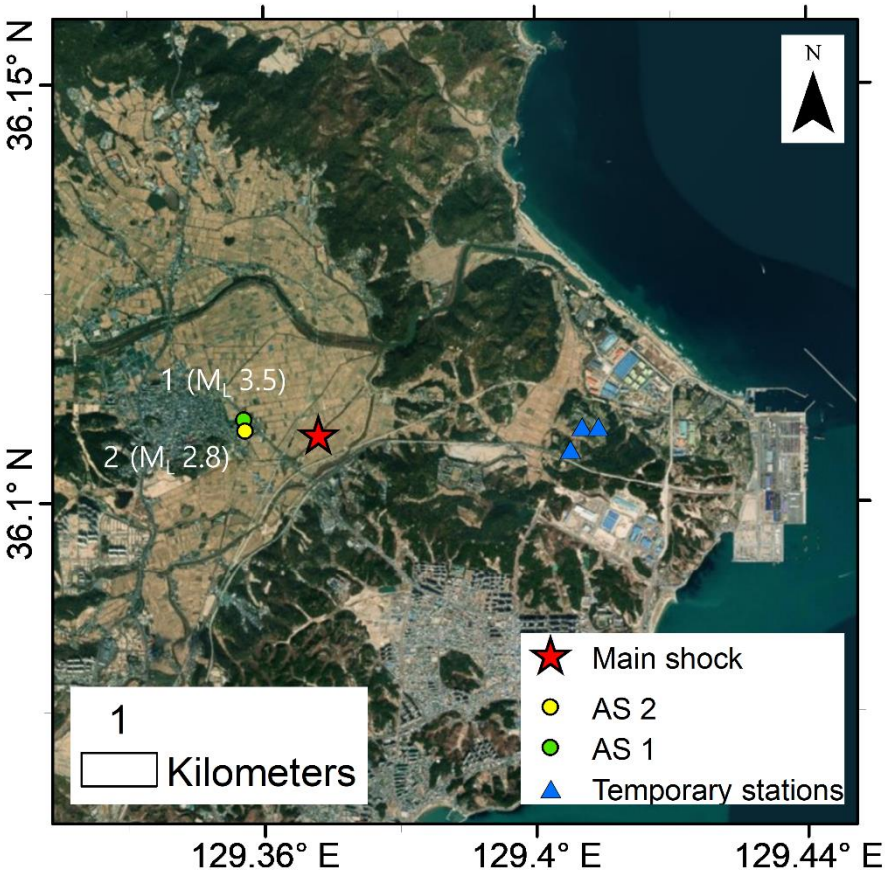

Figure 6. Locations of epicenters of the main shock and two aftershocks (circles), as well as the three temporary seismic stations.

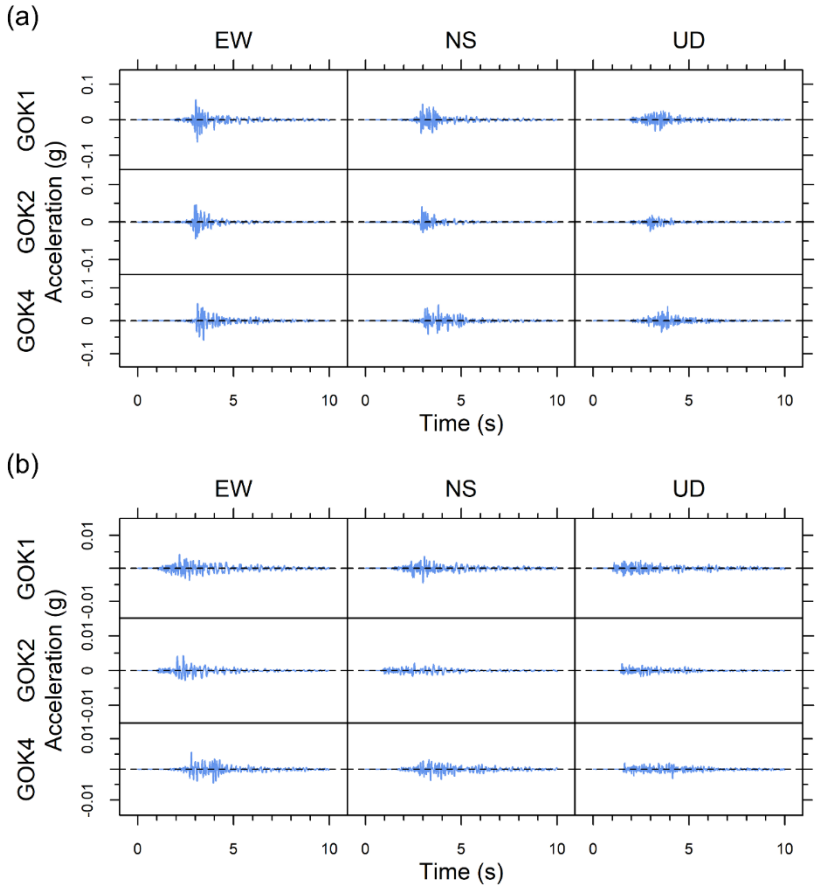

Figure 7. Acceleration time series of (a) Aftershock 1 (M_L 3.5); and (b) Aftershock 2 (M_L 2.8) recorded at three temporary seismic station in east-west (EW), north-south (NS), and up-down (UD) directions.

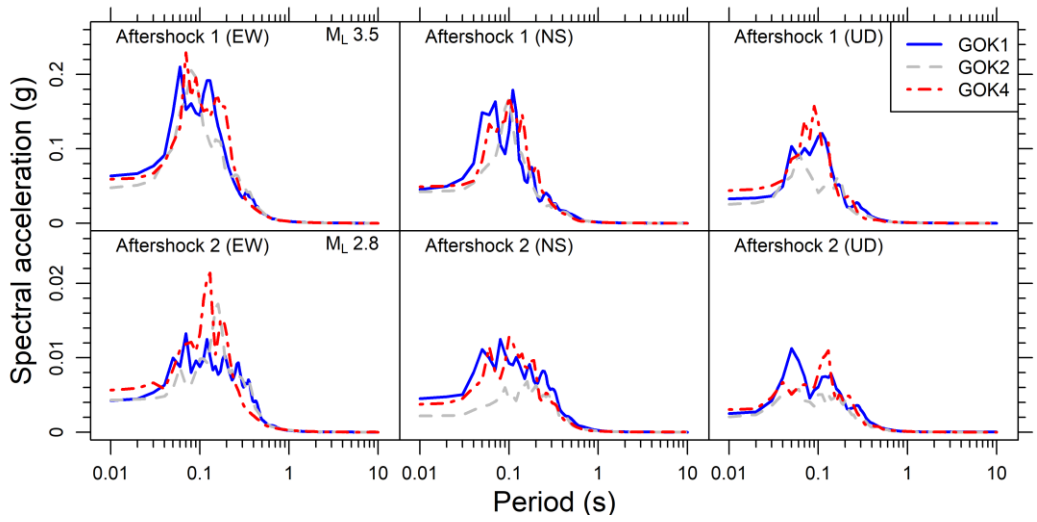

Figure 8. 5% damped spectral acceleration of the ground motions in EW, NS, and UD directions recorded at temporary seismic stations (GOK1, GOK2, and GOK4) during Aftershocks 1 and 2.

4. Numerical analysis

4.1. Previous studies

Numerical analysis to investigate topographic amplification were conducted. Ashford and Sitar (1997) conducted 2D seismic site-response analysis based on the generalized consistent transmitting boundary (GCTB) method

They studied site-response of cliff model with incidence angle on frequency domain. It has an uniform half-space with a shear-wave velocity of 300 m/s, 30m height, a 1% damping, and a Poisson's ratio of 0.3. The incidence angle is measured clockwise from the upward vertical axis. Waves of positive incidence angles propagate away from the slope, and those with negative incidence angles are propagate into the slope. They didn't mention what input motion and angle of slope they used.

They considered The frequencies between 0.1 and 10 Hz for the analyses and calculated amplification in horizontal direction at the crest of a vertical slope (i.e. 90°) respect to free-field behind crest for SV wave with incidence angle ranging from -30 ° to 30 ° and the results were shown in Figure 10.

The model as shown in Figure 9 described Seacliff site located at south of Santa Cruz, California. It has an uniform half-space with a shear-wave velocity of 914 m/s, 27m high bluff with a 75° slope, a 0.5% damping, a Poisson's ratio of 0.3, and incidence angle ranging from 0° to 30°. The incidence angle is measured clockwise from the upward vertical axis. Waves of positive incidence angles propagate away from the slope, and those with negative incidence angles are propagate into the slope.

Three different California earthquakes were used as input motion. The El Centro N/S (ECNS) is from E1 Centro earthquake (M_W = 6.9) recorded on the 18, May, 1940 and it has 0.32 g peak acceleration. The UCSC0 is from Loma Prieta Earthquake (M_S = 7.1) generated on 17 October 1989 and it has 0.42 g peak acceleration. The JOS90 is from Landers earthquake (M_S = 7.5) recorded on the 28 June 1992 and it has 0.28 g peak acceleration. Table 20 shows the peak acceleration at slope crest (a_{max}) and free-field behind the crest (a_{ffc}). Amplification

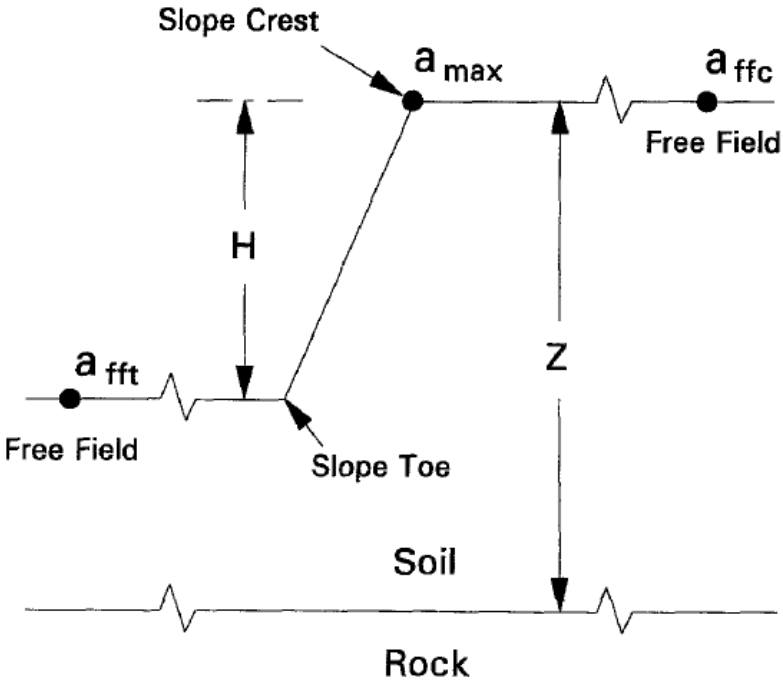

Figure 9. Schematic of seacliff model used in Ashford and Sitar (1997)

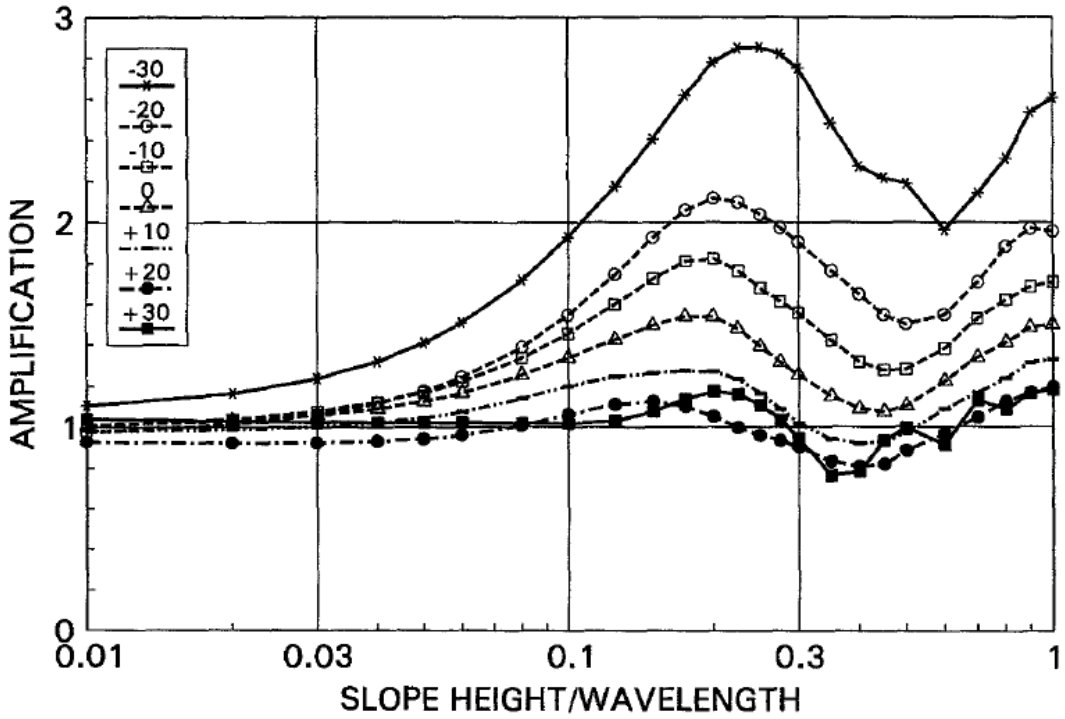

Figure 10. Amplification at the crest of a vertical slope (i.e. 90°) for SV incidence wave (-30 ° to 30 °) (Ashford & Sitar, 1997).

Incident Wave Inclination (deg)	Input Motion	f_t (Hz)	f_n (Hz)	f_{eq} (Hz)	a_{fft} (g)	a_{ffc} (g)	a_{max} (g)	A_t (%)	A_s (%)	A_a (%)
0	ECNS	2.46	3.07	5–6	0.32	0.81	1.15	42	153	259
	UCSC0	2.46	3.07	3, 5–7	0.42	1.12	1.57	40	167	274
	JOS90	2.46	3.07	1, 3–4	0.27	0.51	0.75	47	89	178
10	ECNS	2.46	3.07	5–6	0.31	0.78	1.20	54	152	287
	UCSC0	2.46	3.07	3, 5–7	0.41	1.08	1.69	56	163	312
	JOS90	2.46	3.07	1, 3–4	0.26	0.49	0.77	57	88	196
20	ECNS	2.46	3.07	5–6	0.27	0.62	1.08	74	130	300
	UCSC0	2.46	3.07	3, 5–7	0.36	0.79	1.49	89	119	314
	JOS90	2.46	3.07	1, 3–4	0.22	0.33	0.64	94	50	191
30	ECNS	2.46	3.07	5–6	0.26	0.60	1.07	78	131	312
	UCSC0	2.46	3.07	3, 5–7	0.34	0.74	1.44	94	118	324
	JOS90	2.46	3.07	1, 3–4	0.22	0.32	0.64	100	45	190

Figure 11. Results of simulation in horizontal direction for incidence angle (Ashford & Sitar, 1997).

Assimaki and Gazetas (2004) conducted 2D seismic site-response analysis for the model describing the Kifisos river canyon and the region of Adames. They used Ricker wavelet of type Beta as input motion:

$$\mathrm{u(t)} = [1 - 2b(t - t_0)^2]\exp[-b(t - t_0)^2] \quad (1)$$

where $b = (\pi f_0)^2$, with f_0 as the characteristic frequency, and t_0 is time of max[u(t)].

Two methods were used for 2D wave propagation analyses which were ABAQUS based on the finite-element code and the AHNSE based on spectral-element code. The idealized cross section of the Kifisos river canyon and the region of Adames is shown in Figure 12 as configuration of layered structure. It has homogeneous layer (i.e. $V_{S1} = V_{S2}$) over bedrock (V_{S3}) and it has three different soil properties. the shear velocities for homogeneous layer are 562.5, 500, and 1000 m/s and those for bedrocks are 750, 1000, and 5000 m/s. Its slope angle is 30° and 5% damping applied to the structure. Figure 13 shows depth and shear-wave velocity of layer for parametric study.

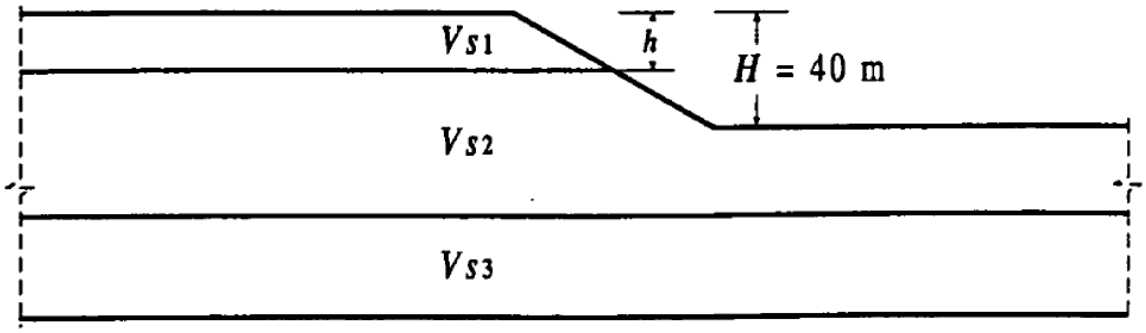

Figure 12. The configuration of layered structure (Assimaki & Gazetas, 2004)

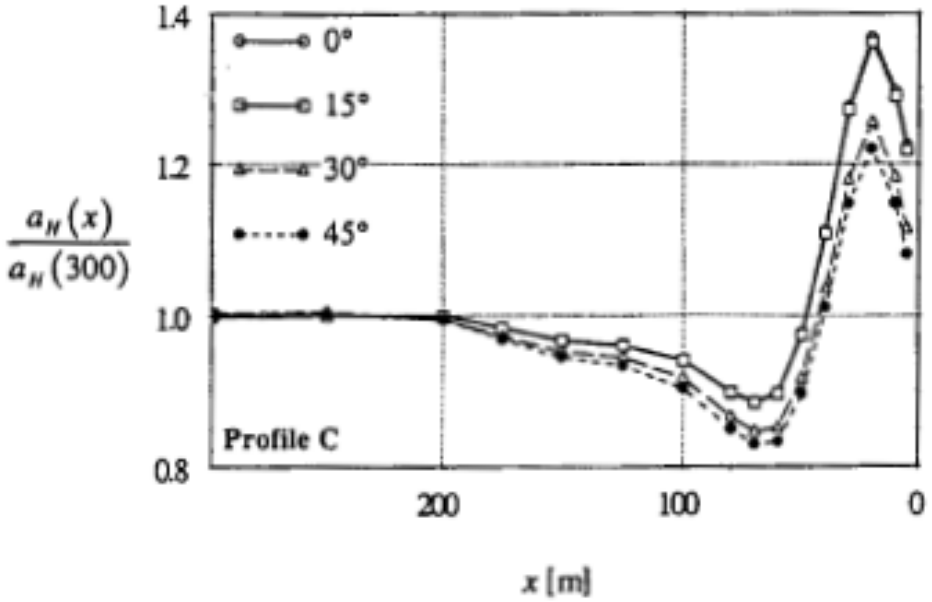

Figure 13. Normalized peak acceleration for the incidence angle of 0°, 15°, 30°, and 45° (Assimaki & Gazetas, 2004)

4.2. Methodology

Simulations of seismic wave propagations for 2D model as shown in Figure 18a were conducted using the finite-difference model, FLAC 2D v.7.0 (Itasca, 2011). The 2D model comprise topographic part and base part. The topographic part have two different profile (i.e., Line-1 and Line-2 as shown in Figure 18b,c and the base part commonly have width of 1500m and height of 708m. Meshes with a size about 2m and 1.5m in x direction and y direction, respectively, were used as shown in Figure 18e,f,g. Free-field boundary conditions were applied to the left and right sides that supplies identical conditions to propagating wave in an infinite model. X direction and y direction quiet boundary conditions were applied to the base of the entire models.

In dynamic problems, fixed or elastic boundaries conditions cause the reflection of outward propagating waves back into the model and do not allow the necessary energy radiation. To prevent the troubles, quiet (or absorbing) boundaries are used. FLAC used the quiet-boundary scheme proposed by Lysmer and Kuhlemeyer (1969). It includes independent dashpots attached to the boundary in the normal and shear directions (Itasca, 2011). Free-field boundaries are used to lateral boundaries to preserve their nonreflecting properties and prevent an energy leaking out. The lateral boundaries are coupled to the free-field grid by viscous dashpots to simulate a quiet boundary (see Figure 16), and the unbalanced forces from the free-field grid are applied to the main-grid boundary (Itasca, 2011). The ground motions of Aftershock 1 and Aftershock 2 in the EW direction measured at GOK2 temporary station were used as input incident SV waves (Figure 18,h). Input waves were scaled so that the estimated PGAs of Aftershock 1 and Aftershock 2 at GOK2 agree with the measured PGAs.

To apply seismic wave on a quiet boundary, a stress boundary condition is used. Acceleration records were changed into velocity records. Subsequently, the velocity records were transformed into stress records using the formula:

$$\sigma_n = \rho C_p v_n \quad (2)$$

$$\sigma_s = \rho C_s v_s \quad (3)$$

where σ_n = applied normal stress, σ_s = applied shear stress, ρ = mass density, C_p = speed of p-wave propagation through medium, C_s = speed of s-wave propagation through medium, v_n = input normal particle velocity, and v_s = input shear particle velocity (Itasca, 2011).

4.3. Topography model

Two different models (2-layer model and 4-layer model) were considered: (1) 2-layer model: a two-layers domain with V_S values of 200 and 350 m/s for the near-surface layer (soil 1 with a 5m depth) and the lower layer (soil 2), respectively; (2) 4-layer model : a four-layer domain with V_S values of 165, 170, 220, and 340 m/s for the near-surface layer (soil 1 with a 2m depth), the second layer from a surface (soil 2 with a 2m depth), the third layer from a surface (soil 3 with a 3m depth), and the lowest layer (soil 4), respectively.

SV-waves approaching the ground surface at critical angle generate reflected SV-waves and P-waves propagating along the surface as shown in Figure 17a. As shown in Figure 17b, when the reflected SV-waves and P-waves propagating along the surface generated by SV-waves propagating to slope encounter the direct SV-wave behind the crest simultaneously, those generate superposition of waves. (Assimaki et al., 2005). Kang et al. (2019b) calculated the critical angles for the slope of the Gokgang-ri are about 10° ~ 20° using critical angles for flat ground (20° ~ 26°) and slope angle of Gokgang-ri (6° ~ 10°). The incidence angles of two aftershocks (AS 1 and AS 2) were calculated using the crustal P velocity used by Hong et al. (2017). The incidence angles of AS 1 and AS2 were calculated considering

P velocity profile (0-0.15km: 3.7km/s; 0.15-1km: 4.84 km/s; 1-3km: 5.55 km/s; 3-6km: 5.85 km/s; 6-10km: 6.05 km/s;), depth of the aftershocks (AS 1: 7.9km; AS 2: 9.5km) and distance from the aftershocks to study area (~4.5km) and the values are approximately 19° and 16° for AS 1 and AS 2, respectively. As a result, incidence angles of input motion for numerical simulations were considered up to 20°.

Amplitudes of input motions used in this study are not large, and the surface layers are stiff enough. Therefore, we conduct linear analyses with soils' damping ratios of 5% and 1% as shown in Table 2 and Table 3.

Free-field profiles (without surface topographies) for both Line-1 and Line-2 of the 2 different model were also simulated and estimated motions of ground surface of free-field were used as reference for amplification factors.

The result of 1D simulation using FLAC 2D was compared with those using DEEPSOIL v.7.0. which is a one-dimensional site response analysis program prior to simulation of 2D topographic profiles. Meshes with a size 0.5m in x and y directions were used in FLAC 2D model. Free-field boundary and x and y direction quiet boundary were applied to the left and right sides and the base line of the model, respectively. FLAC 2D and DEEPSOIL models have a height of 100m and 4-layer as shown in Figure 14 (i.e., V_S value: 165, 170, 220, and 340 m/s for Soil 1, Soil 2, Soil 3 and Soil 4, respectively). The ground motion of Aftershock 1 measured at GOK2 temporary station in EW direction for a duration of 3 s were used as input SV wave. Linear elastic material properties with a damping ratio of 5% and 1% were applied as shown in Table 3. The acceleration times series and spectral acceleration, from the both software program are similar as shown in Figure 15.

Table 2. Properties of 2-layer model.

2-layer model					
Layer	V_S (m/s)	Poisson's ratio	Shear modulus (Pa)	Damping Ratio (%)	f_{min} and f_{max} (Hz) for Rayleigh damping
Soil 1	200	0.4239	89704383	5	3 and 15
Soil 2	350	0.4318	274719674	1	3 and 15

Table 3. Properties of 4-layer model.

4-layer model					
Layer	V_S (m/s)	Poisson's ratio	Shear modulus (Pa)	Damping Ratio (%)	f_{min} and f_{max} (Hz) for Rayleigh damping
Soil 1	165	0.4239	61055046	5	3 and 15
Soil 2	175	0.4239	64811417	5	3 and 15
Soil 3	220	0.4239	151600408	5	3 and 15
Soil 4	340	0.4318	259245668	1	3 and 15

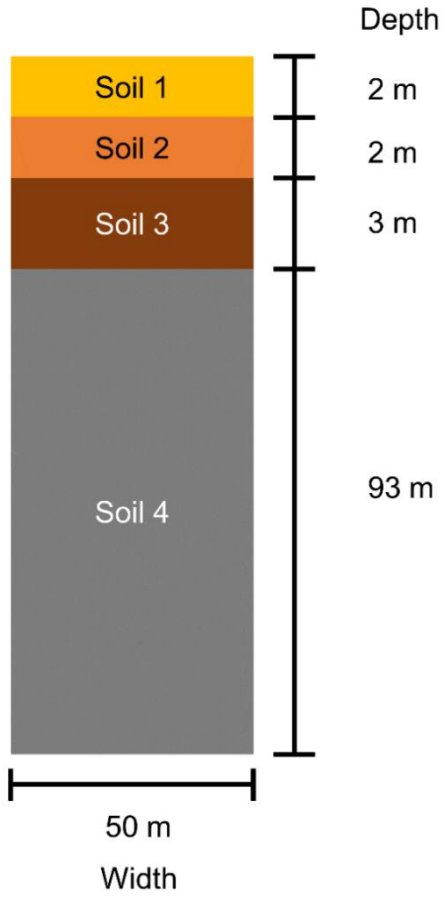

Figure 14. Layered structure of 1D simulation model

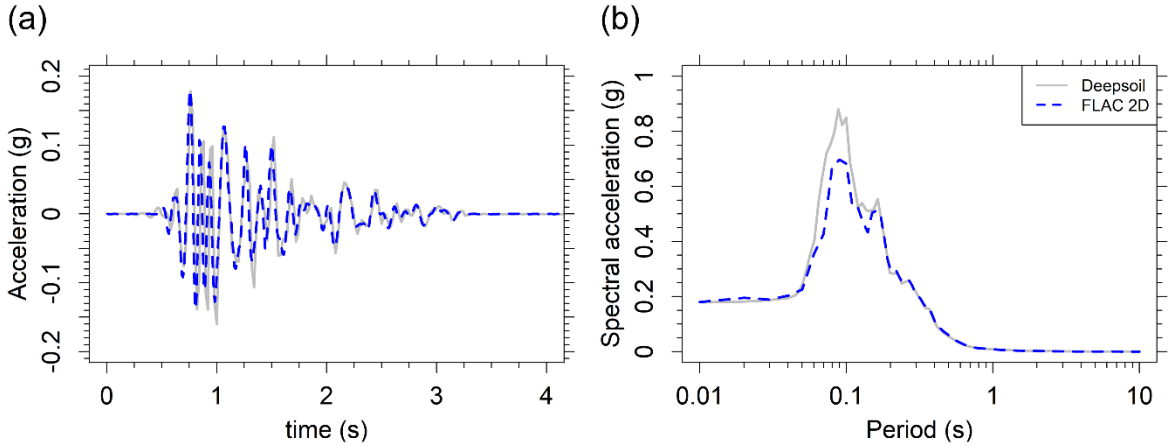

Figure 15. (a) Acceleration time series and (b) Spectral acceleration of 1D response results simulated by DEEPSOIL and FLAC 2D.

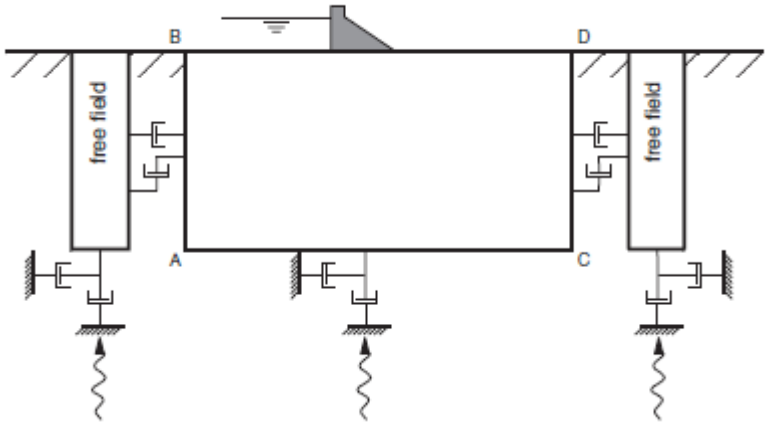

Figure 16. Model for seismic analysis of surface structures and free-field mesh (Itasca, 2011)

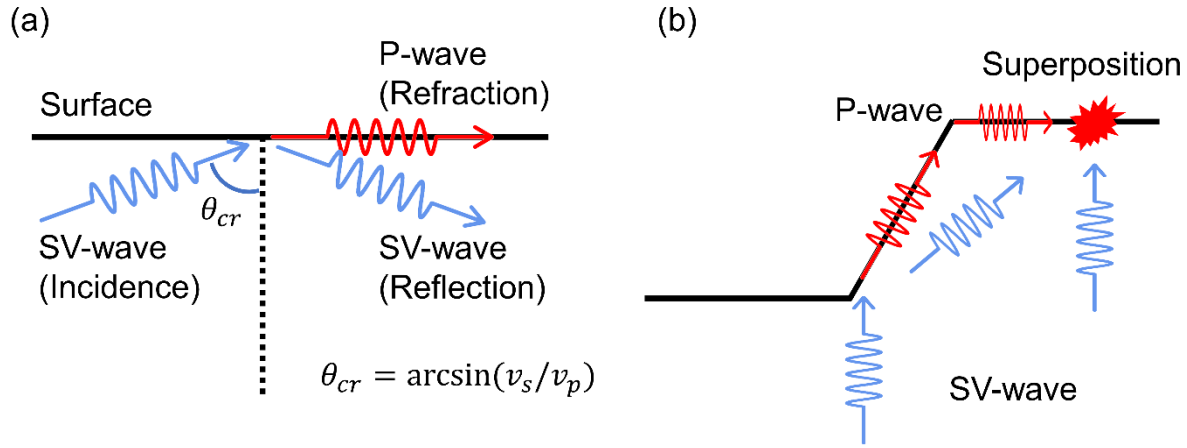

Figure 17. Schematic diagram of (a) critical angle and (b) topographic effect by the wave propagating at critical angle to the surface of slope.

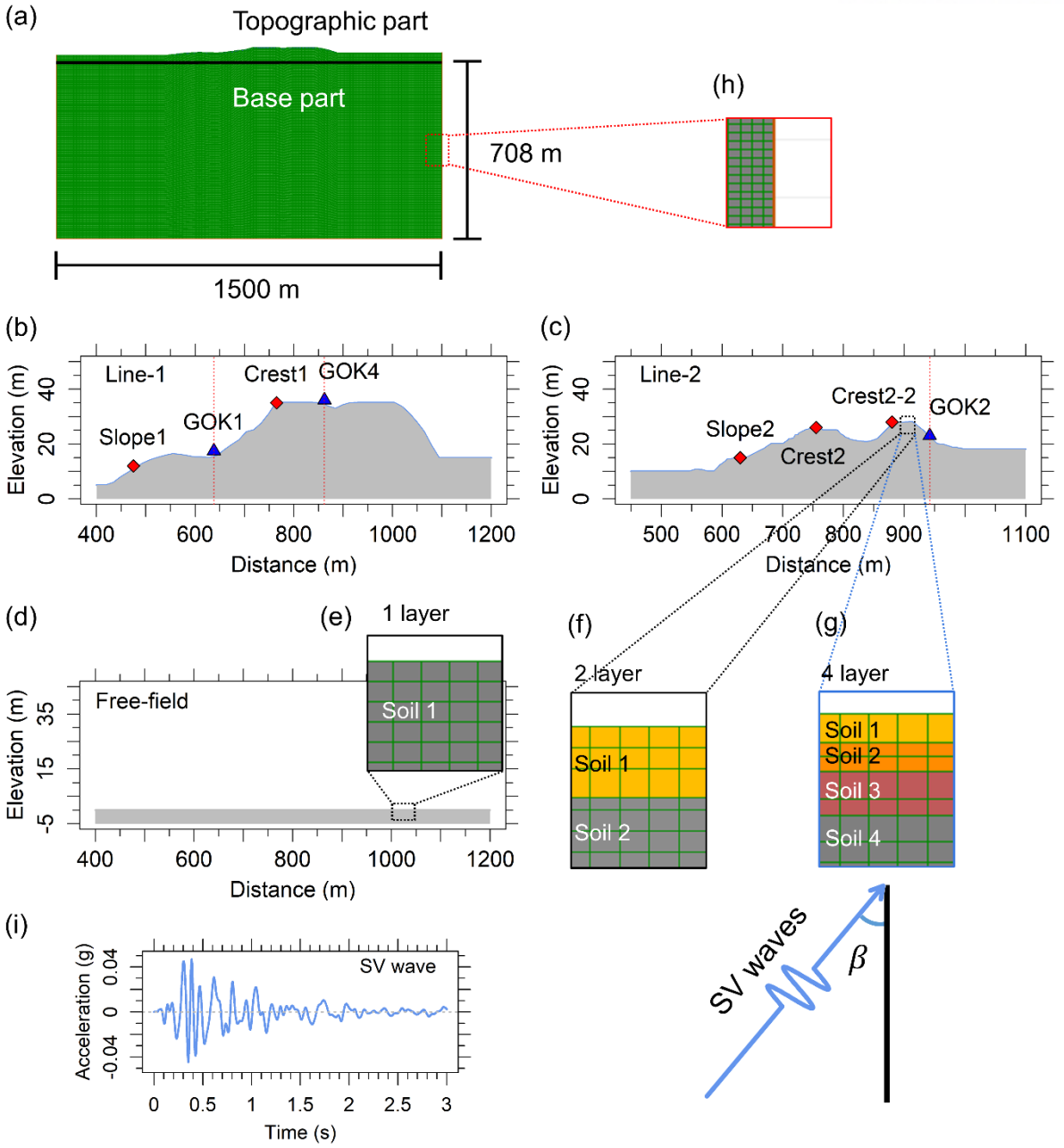

Figure 18. (a) Dimension of 2D model used in numerical simulation. (b, c) Topographic profiles used for Topographic part in a west–east direction at Line-1 and Line-2, respectively. (d) Free-field profiles in west-east direction. (e) Meshes of the free-field numerical model near the ground surface. (f) Meshes of the 2-layer numerical model near the ground surface. (g) Meshes of the 4-layer numerical model near the ground surface. (h) Close-up meshes that free-field boundary applied to. (i) Acceleration time series of the incident SV wave.

5. Result

5.1. 2-layer model

Figure 19 shows acceleration time series of the estimated ground motions for the 2-layer model using Aftershock 1 as input motion in a horizontal direction at GOK1, GOK2, and GOK4 for four different incidence angles: 0°, 10°, 15°, and 20°. In general, the estimated ground motions match well with the ground motions measured in the EW direction. It can be noticed that the PGAs are largest when the incidence angle is 15°. Figure 20 shows 5% damped spectral acceleration of estimated ground motion corresponding to Figure 19. PGAs at GOK2 were slightly smaller than those at GOK1 and GOK4 for all incidence angle, and PGAs at each station for 15° are maximum value (i.e., 0.051 (g) at GOK1, 0.045 (g) at GOK2, and 0.055 (g) at GOK4). PGAs, Sas at a period of 0.1s and Sas at a period of 1s at the temporary stations (GOK1, GOK2, and GOK4) for the 10° and 15° are generally lager than those for 0° and 20°.

Figure 21 shows PGA and Sa values at 0.1 s and 1 s estimated along Line-1 and Line-2. The PGA and Sa values are estimated to be larger on the slopes or plateaus facing the epicenter than those on the slope of opposite direction. The PGA and Sa values are generally larger when the incidence angle is 15° than for other incidence angles. The value of PGA and Sa at 0.1s and 1s are shown in Table 4, Table 5, and Table 6.

Figure 22 shows amplification factors which are defined as ratios of Sa values estimated at the topography models (Sa^{topo}) to those estimated at the free-field model ($Sa^{free\text{-}field}$) for three periods (i.e., PGA, 0.1 s and 1 s). It can be noticed that the Sa values at the slope near the point where the slope begins to rise (toe of slope) and crests of the slopes facing the epicenter are larger than those at the slopes facing in the opposite direction. The maximum amplifications of PGA (PGA^{topo} / $PGA^{free\text{-}field}$) range from approximately 1.34 to 1.54 at the slope and crests. The maximum amplifications of Sa at 0.1 s (Sa^{topo} / $Sa^{free\text{-}field}$ at period of 0.1s) range from approximately 1.47 to 1.9 at the Slopes and Crests. The amplifications of Sa at 1 s (Sa^{topo} / $Sa^{free\text{-}field}$ at period of 1s) fluctuate on the unity.

The amplification factors for PGA and Sa at 0.1 s at Slopes, Crests, GOK1 and GOK4 are generally larger than those at GOK2. At GOK1, the amplification factors for PGA and Sa at 0.1 s are the largest when the incidence angle is 0 and 10°, respectively. At GOK4, the amplification factors for PGA and Sa at 0.1 s are the largest when the incidence angle is 15° and 10°, respectively. The amplification factors at two Slopes and Crest1 and 2 for PGA and Sa at 0.1 s are the smallest when the incidence angle is 0°. However those at Crest2-2 are the smallest for the incidence angle of 20°. The differences between the maximum amplifications at the slope crest and the minimum amplifications on the opposite slope are larger for the incidence angles of 15° and 20° than for 0 and 10°. The values of amplification factors of PGA, Sa at periods of 0.1s and 1 s are shown in Table 7, Table 8 and Table 9.

Figure 23 shows the Sas estimated for GOK1 (Sa_1) and GOK4 (Sa_4) normalized by those

estimated for GOK2 (Sa_2), respectively, with period for four incidence angle. The ratios are generally greater than the unity. At periods of 0.01 s – 0.04 s, the ratios are always greater than the unity, and those for incidence angles of 10 and 15 are greater than those for incidence angles of 0 and 20 for both (Sa_1/Sa_2 and Sa_4/Sa_2). In addition, when the incidence angels are 10 and 15, the ratios greater than the unity at periods longer than 0.3 s.

Table 4. PGA for Estimated acceleration of 2-layer model using Aftershock 1 as input in a horizontal direction at a location of GOK1, GOK2, and GOK4 for four different incidence angles (0°, 10°, 15°, and 20°).

PGA (g)				
	0°	10°	15°	20°
GOK1	0.049	0.05	0.051	0.046
GOK2	0.045	0.044	0.045	0.044
GOK4	0.049	0.052	0.055	0.049
Slope1	0.052	0.062	0.069	0.064
Crest1	0.056	0.059	0.064	0.057
Slope2	0.056	0.061	0.068	0.064
Crest2	0.052	0.055	0.059	0.053
Crest2-2	0.056	0.061	0.062	0.052

Table 5. Sa at 0.1s for Estimated acceleration of 2-layer model using Aftershock 1 as input in a horizontal direction at a location of GOK1, GOK2, and GOK4 for four different incidence angles (0°, 10°, 15°, and 20°).

Sa at 0.1s (g)				
	0°	10°	15°	20°
GOK1	0.185	0.208	0.195	0.168
GOK2	0.164	0.179	0.184	0.154
GOK4	0.186	0.197	0.196	0.18
Slope1	0.19	0.23	0.276	0.286
Crest1	0.222	0.215	0.231	0.197
Slope2	0.211	0.239	0.263	0.25
Crest2	0.201	0.205	0.221	0.196
Crest2-2	0.2	0.211	0.213	0.197

Table 6. Sa at 1s for Estimated acceleration of 2-layer model using Aftershock 1 as input in a

horizontal direction at a location of GOK1, GOK2, and GOK4 for four different incidence angles (0°, 10°, 15°, and 20°).

Sa at 1s (g)				
	0°	10°	15°	20°
GOK1	0.003	0.004	0.004	0.003
GOK2	0.003	0.003	0.003	0.003
GOK4	0.003	0.003	0.004	0.003
Slope1	0.004	0.005	0.004	0.003
Crest1	0.004	0.004	0.004	0.003
Slope2	0.003	0.004	0.004	0.003
Crest2	0.004	0.004	0.004	0.003
Crest2-2	0.004	0.003	0.003	0.003

Table 7. Amplification factor of PGA for estimated acceleration of 2-layer model using Aftershock 1 as input in a horizontal direction at a location of GOK1, GOK2, and GOK4 for four different incidence angles (0°, 10°, 15°, and 20°).

Amplification factor of PGA				
	0°	10°	15°	20°
GOK1	1.263	1.202	1.108	1.123
GOK2	1.16	1.114	1.091	1.227
GOK4	1.282	1.296	1.336	1.27
Slope1	1.352	1.444	1.458	1.428
Crest1	1.457	1.467	1.506	1.512
Slope2	1.459	1.481	1.466	1.498
Crest2	1.34	1.365	1.408	1.395
Crest2-2	1.451	1.541	1.464	1.397

Table 8. Amplification factor of Sa at 0.1s for Estimated acceleration of 2-layer model using Aftershock 1 as input in a horizontal direction at a location of GOK1, GOK2, and GOK4 for four different incidence angles (0°, 10°, 15°, and 20°).

Amplification factor of Sa at 0.1s				
	0°	10°	15°	20°
GOK1	1.496	1.565	1.328	1.21
GOK2	1.324	1.426	1.356	1.185

GOK4	1.5	1.526	1.39	1.372
Slope1	1.537	1.748	1.871	1.877
Crest1	1.791	1.631	1.558	1.527
Slope2	1.701	1.725	1.794	1.828
Crest2	1.619	1.542	1.499	1.473
Crest2-2	1.615	1.644	1.577	1.526

Table 9. Amplification factor of Sa at 1s PGA for Estimated acceleration of 2-layer model using Aftershock 1 as input in a horizontal direction at a location of GOK1, GOK2, and GOK4 for four different incidence angles (0°, 10°, 15°, and 20°).

Amplification factor of Sa at 1s				
	0°	10°	15°	20°
GOK1	0.946	0.848	1.046	1.054
GOK2	0.976	1.071	0.972	1.175
GOK4	0.971	1.026	1.116	0.949
Slope1	1.079	1.213	0.99	1.009
Crest1	1.112	1.084	1.23	1.269
Slope2	1.041	1.11	1.06	1.091
Crest2	1.055	1.068	1.116	1.397
Crest2-2	1.044	1.153	1.199	1.23

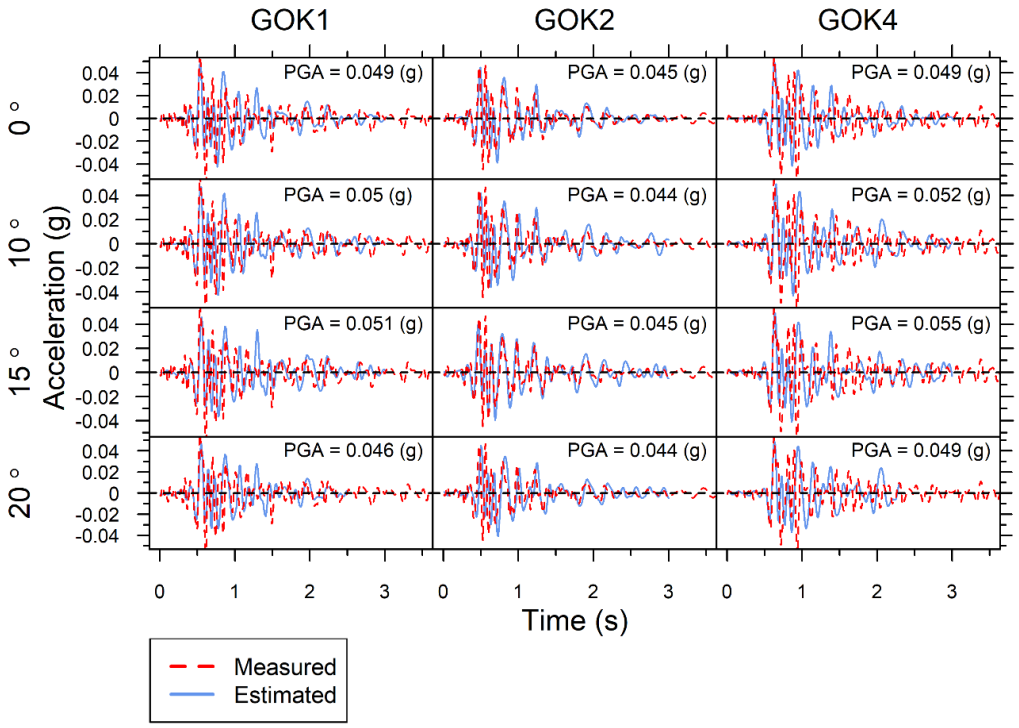

Figure 19. Estimated acceleration time series in a horizontal direction for the 2-layer model using Aftershock 1 as input wave at GOK1, GOK2, and GOK4 for four different incidence angles (0°, 10°, 15°, and 20°). The measured acceleration time series of Aftershock 1 in the EW direction are also presented.

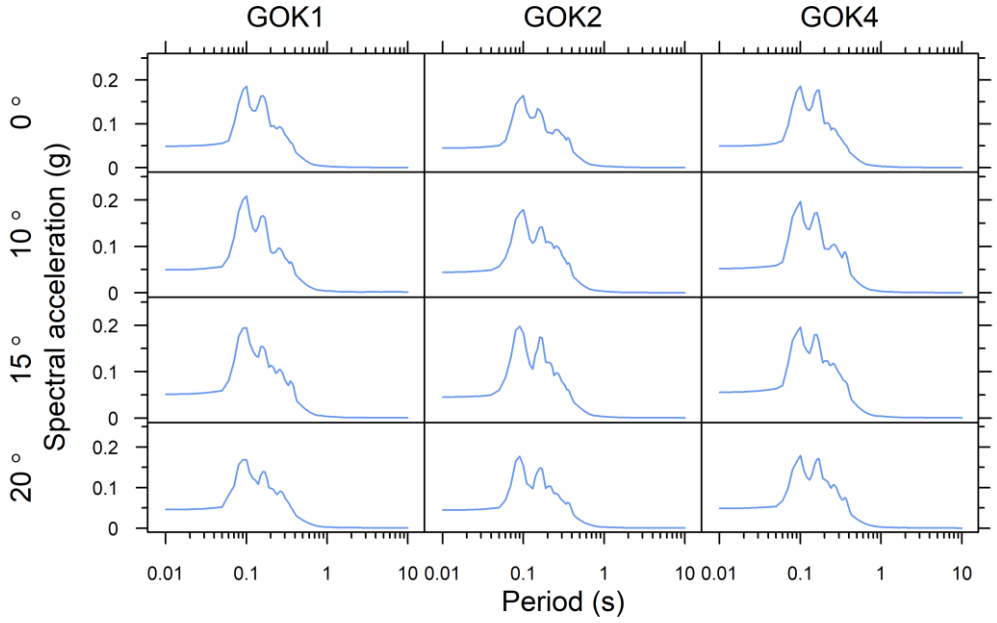

Figure 20. Estimated spectral acceleration in a horizontal direction for the 2-layer model using Aftershock 1 as input wave at GOK1, GOK2, and GOK4 for four different incidence angles.

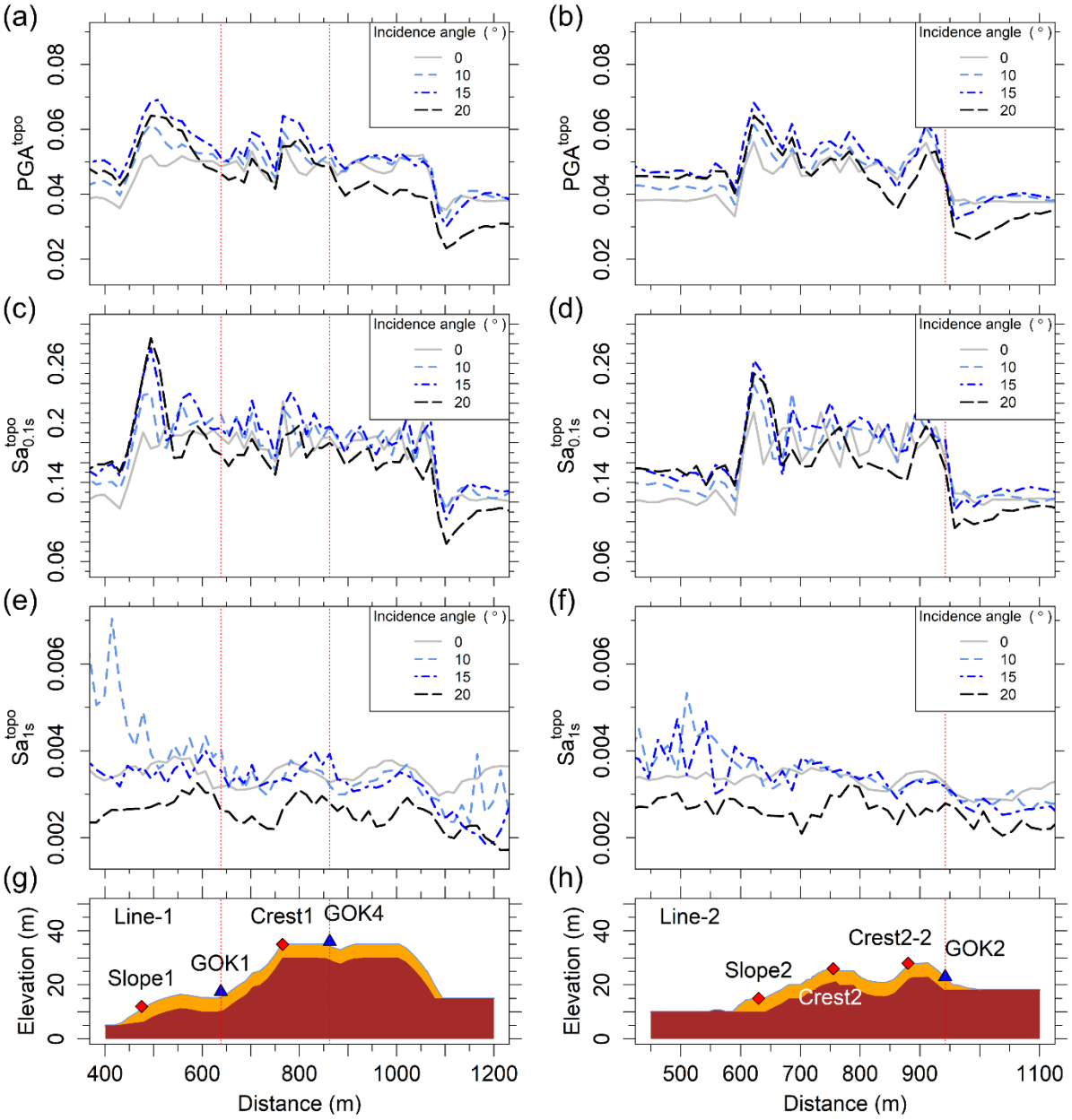

Figure 21. (a,b) PGA, (c,d) Sa at period of 0.1s, and (e,f) Sa at period of 1s of 2-layer model using Aftershock 1 as input wave in a horizontal direction on the ground surfaces of Line-1 and line-2 relative to the free-field, respectively, for four different incidence angles (0°, 10°, 15°, and 20°).

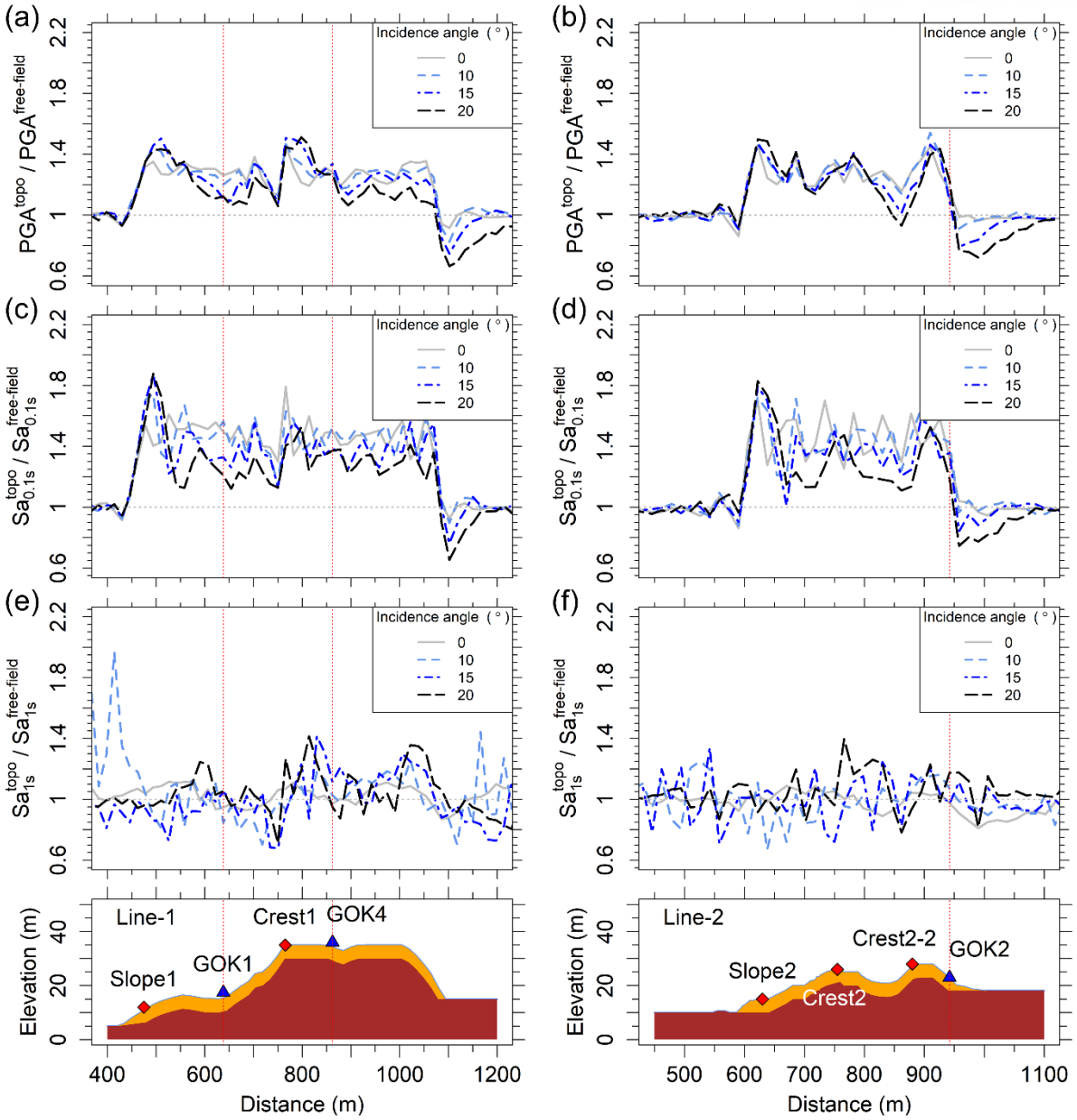

Figure 22. Amplification factors with respect to the free-field responses: (a, b) amplification factors of PGA (i.e., $PGA^{topo}/PGA^{free\text{-}field}$), (c,d) amplification factors of Sa at 0.1s (i.e., $Sa_{0.1s}{}^{topo}/Sa_{0.1s}{}^{free\text{-}field}$), and (e,f) Sa at a period of 1s (i.e., $Sa_{1s}{}^{topo}/Sa_{1s}{}^{free\text{-}field}$) for the 2-layer models (Line-1 and Line-2, respectively) using the EW motion from Aftershock 1 as an input wave motion with four different incidence angles (0°, 10°, 15°, and 20°).

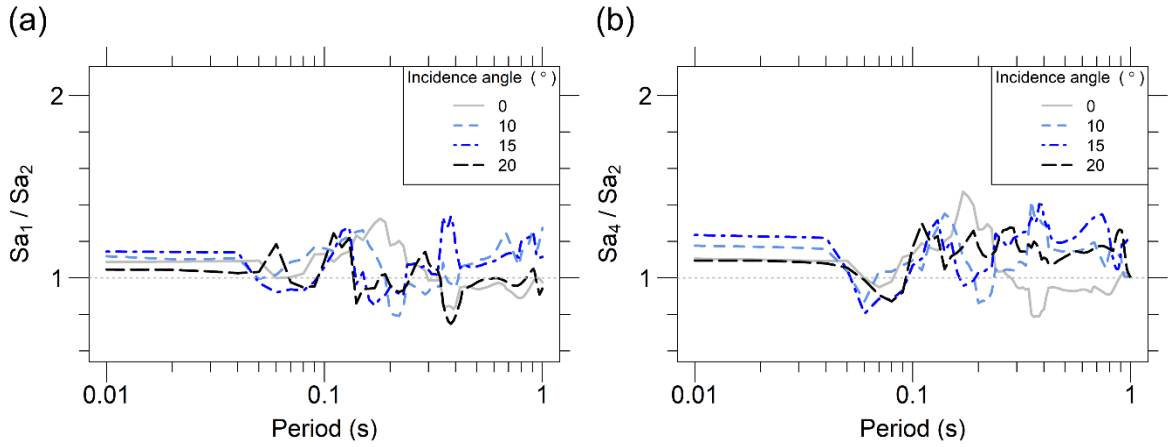

Figure 23. Ratio of the simulated Sas of 2-layer model using Aftershock 1 as input wave at GOK1 and GOK4 to those at GOK2 in a horizontal direction for four different incidence angles (0°, 10°, 15°, and 20°): (a) GOK1 to GOK2; (b) GOK4 to GOK2.

Figure 24 shows the acceleration time series of the estimated ground motions for the 2-layer model using Aftershock 2 as input motion in a horizontal direction at GOK1, GOK2, and GOK4 for four different incidence angles: 0°, 10°, 15°, and 20°. The estimated ground motion at GOK2 matches well with recorded ground motion however The estimated ground motions at GOK1 and GOK4 are slightly different with recorded ground motions.

Figure 25 shows the 5% damped spectral acceleration of estimated ground motion corresponding to Figure 24. Similar with result of 2-layer model using Aftershock1 as input motion. Figure 24 show that PGAs at GOK1 and GOK4 are slightly larger than those at GOK2. PGAs for 10° generally larger than those for other incidence angles.

Figure 26 shows PGA and Sa values at 0.1 s and 1 s estimated along Line-1 and Line-2. The PGA and Sa values are estimated to be larger on the slopes or plateaus facing the epicenter than those on the slope of opposite direction. The PGA and Sa values at crest of the slope are generally larger when the incidence angle is 15° and 20° than for other incidence angles. The PGA and Sa values at GOK1 and GOK4 are generally larger when the incidence angle is 10° and 15° than for other incidence angles. The values of PGA and Sa at period of 0.1s and 1s are shown in Table 10, Table 11, and Table 12.

Figure 27 shows amplification factors which are defined as ratios of Sa values estimated at the topography models (Sa^{topo}) to those estimated at the free-field model ($Sa^{free\text{-}field}$) for three periods (i.e., PGA, 0.1 s and 1 s). The maximum amplifications of PGA (PGA^{topo} / $PGA^{free\text{-}field}$) range from approximately 1.28 to 1.5 for four different incidence angles at Crests and Slopes. The maximum amplifications of Sa at 0.1 s (Sa^{topo} / $Sa^{free\text{-}field}$ at period of 0.1s) range from approximately 1.35 to 1.76 for four different incidence angles at Crests and Slopes. It shows that the Sa values at the Crests and Slopes facing the epicenter are larger than those at the slopes facing in the opposite direction. The

amplifications of Sa at 1 s (Sa^{topo} / $Sa^{free\text{-}field}$ at period of 1s) generally fluctuate on the unity.

Table 13, Table 14, and Table 15 show the amplification factors of PGA, Sa at periods of 0.1s and 1 s for the 2-layer model using Aftershock 2's EW record as an input motion, respectively. The amplification factors for PGA and Sa at 0.1 s at Slopes, Crests, GOK1 and GOK4 are generally larger than those at GOK2. The amplification factors for PGA and Sa at 0.1 s at the Slope1 and Slope2 for 15°, and 20° are generally larger than those for 0° and 10°. At GOK1 and GOK4, the amplification factors for PGA and Sa at 0.1 s for 0° and 10° are generally the larger than those for 15°and 20°. The differences between the maximum amplifications at the slope crest and the minimum amplifications on the opposite slope are larger for the incidence angles of 15° and 20° than for 0 and 10°.

Figure 28 shows the Sas estimated for GOK1 (Sa_1) and GOK4 (Sa_4) normalized by those estimated for GOK2 (Sa_2), respectively, with period ranging from 0.01 to 1s for four incidence angle. The ratios are generally greater than the unity. At periods of 0.01 s – 0.08 s, the ratios are always greater than the unity except for Sa_1/Sa_2 of 15°and 20°, and those for incidence angles of 10 and 15 are greater than those for incidence angles of 0° and 20° for both (Sa_1/Sa_2 and Sa_4/Sa_2). In addition, the ratios for incidence angles of 10° and 15° show the greater increase of ratio than those for incidence angles of 0° and 20° at periods longer than 0.1 s.

Table 10. PGA for Estimated acceleration of 2-layer model using Aftershock 2 as input in a horizontal direction at a location of GOK1, GOK2, and GOK4 for four different incidence angles (0°, 10°, 15°, and 20°).

PGA (g)				
	0°	10°	15°	20°
GOK1	0.0048	0.0046	0.0042	0.0039
GOK2	0.0042	0.0042	0.0041	0.0041
GOK4	0.0048	0.0051	0.0045	0.0045
Slope1	0.0051	0.0051	0.0053	0.0053
Crest1	0.0058	0.0054	0.0055	0.0051
Slope2	0.0052	0.0055	0.0055	0.0054
Crest2	0.0051	0.0054	0.0054	0.0051
Crest2-2	0.0058	0.0058	0.0051	0.0045

Table 11. Sa at 0.1s for Estimated acceleration of 2-layer model using Aftershock 2 as input in a horizontal direction at a location of GOK1, GOK2, and GOK4 for four different incidence angles (0°, 10°, 15°, and 20°).

Sa at 0.1s (g)

	0°	10°	15°	20°
GOK1	0.009	0.0106	0.0085	0.008
GOK2	0.0074	0.0083	0.0084	0.0074
GOK4	0.0095	0.0095	0.0083	0.0089
Slope1	0.0093	0.0119	0.012	0.013
Crest1	0.0104	0.0111	0.011	0.011
Slope2	0.0105	0.012	0.0122	0.0124
Crest2	0.0097	0.0097	0.0099	0.01
Crest2-2	0.01	0.0111	0.0105	0.0093

Table 12. Sa at 1s for Estimated acceleration of 2-layer model using Aftershock 2 as input in a horizontal direction at a location of GOK1, GOK2, and GOK4 for four different incidence angles (0°, 10°, 15°, and 20°).

Sa at 1s (g)				
	0°	10°	15°	20°
GOK1	5.00E-04	0.0014	7.00E-04	8.00E-04
GOK2	5.00E-04	8.00E-04	7.00E-04	7.00E-04
GOK4	4.00E-04	8.00E-04	8.00E-04	7.00E-04
Slope1	8.00E-04	0.0019	0.001	8.00E-04
Crest1	4.00E-04	0.0016	8.00E-04	9.00E-04
Slope2	5.00E-04	0.0011	8.00E-04	8.00E-04
Crest2	4.00E-04	8.00E-04	7.00E-04	8.00E-04
Crest2-2	5.00E-04	8.00E-04	7.00E-04	8.00E-04

Table 13. Amplification factor of PGA for Estimated acceleration of 2-layer model using Aftershock 2 as input in a horizontal direction at a location of GOK1, GOK2, and GOK4 for four different incidence angles (0°, 10°, 15°, and 20°).

Amplification factor of PGA				
	0°	10°	15°	20°
GOK1	1.216	1.165	1.058	1.061
GOK2	1.047	1.045	1.156	1.182
GOK4	1.201	1.283	1.181	1.268
Slope1	1.287	1.353	1.422	1.378
Crest1	1.46	1.394	1.399	1.382

Slope2	1.301	1.392	1.412	1.446
Crest2	1.289	1.386	1.375	1.38
Crest2-2	1.459	1.466	1.369	1.28

Table 14. Amplification factor of Sa at 0.1s for Estimated acceleration of 2-layer model using Aftershock 2 as input in a horizontal direction at a location of GOK1, GOK2, and GOK4 for four different incidence angles (0°, 10°, 15°, and 20°).

Amplification factor of Sa at 0.1s				
	0°	10°	15°	20°
GOK1	1.306	1.312	1.188	1.138
GOK2	1.069	1.232	1.301	1.139
GOK4	1.403	1.414	1.192	1.257
Slope1	1.361	1.594	1.644	1.757
Crest1	1.492	1.616	1.53	1.543
Slope2	1.524	1.596	1.651	1.623
Crest2	1.403	1.423	1.29	1.416
Crest2-2	1.426	1.582	1.519	1.444

Table 15. Amplification factor of Sa at 1s PGA for Estimated acceleration of 2-layer model using Aftershock 2 as input in a horizontal direction at a location of GOK1, GOK2, and GOK4 for four different incidence angles (0°, 10°, 15°, and 20°).

Amplification factor of Sa at 1s				
	0°	10°	15°	20°
GOK1	1.152	0.672	1.131	0.901
GOK2	1.342	0.964	0.791	0.965
GOK4	0.704	0.98	0.87	0.567
Slope1	1.704	1.204	0.728	1.211
Crest1	1.061	1.406	1.242	1.245
Slope2	1.271	1.076	1.139	1.143
Crest2	0.915	0.668	1.059	1.336
Crest2-2	1.082	1.142	1.007	1.166

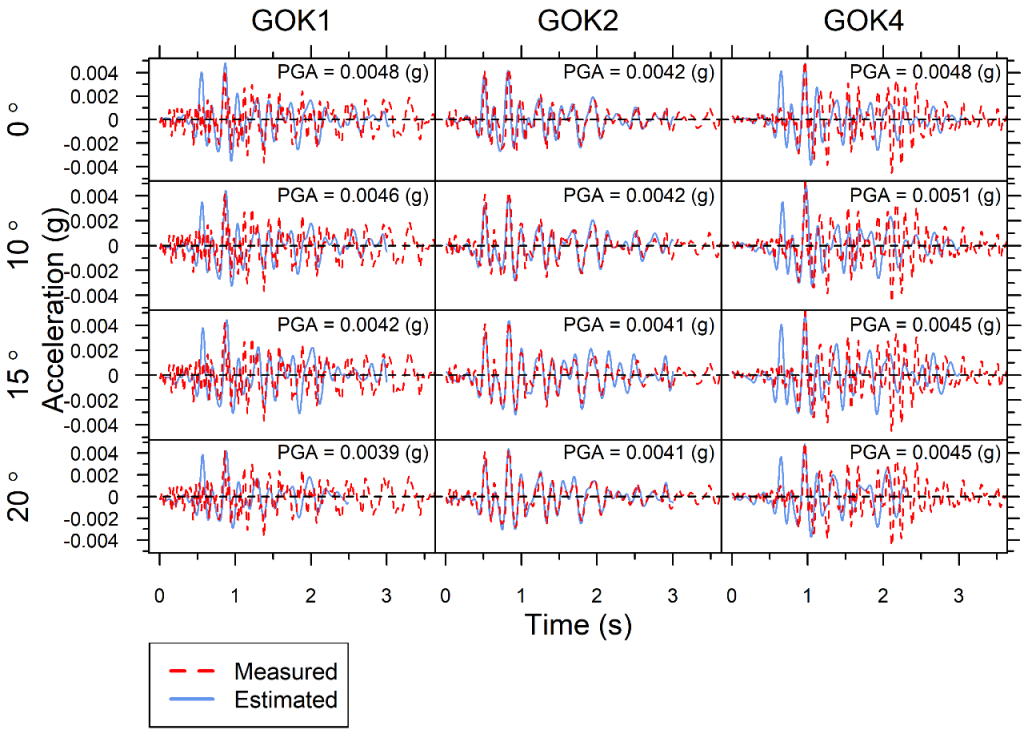

Figure 24. Estimated acceleration time series in a horizontal direction for the 2-layer model using Aftershock 2 as input wave at GOK1, GOK2, and GOK4 for four different incidence angles (0°, 10°, 15°, and 20°). The measured acceleration time series of Aftershock 2 in the EW direction are also presented.

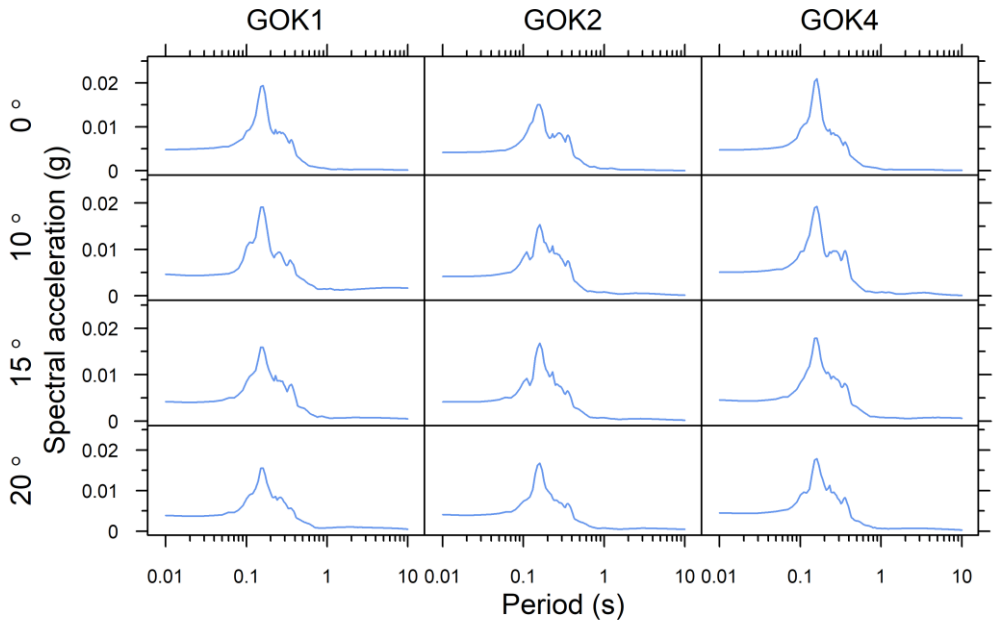

Figure 25. Estimated spectral acceleration in a horizontal direction for the 2-layer model using Aftershock 2 as input wave at GOK1, GOK2, and GOK4 for four different incidence angles.

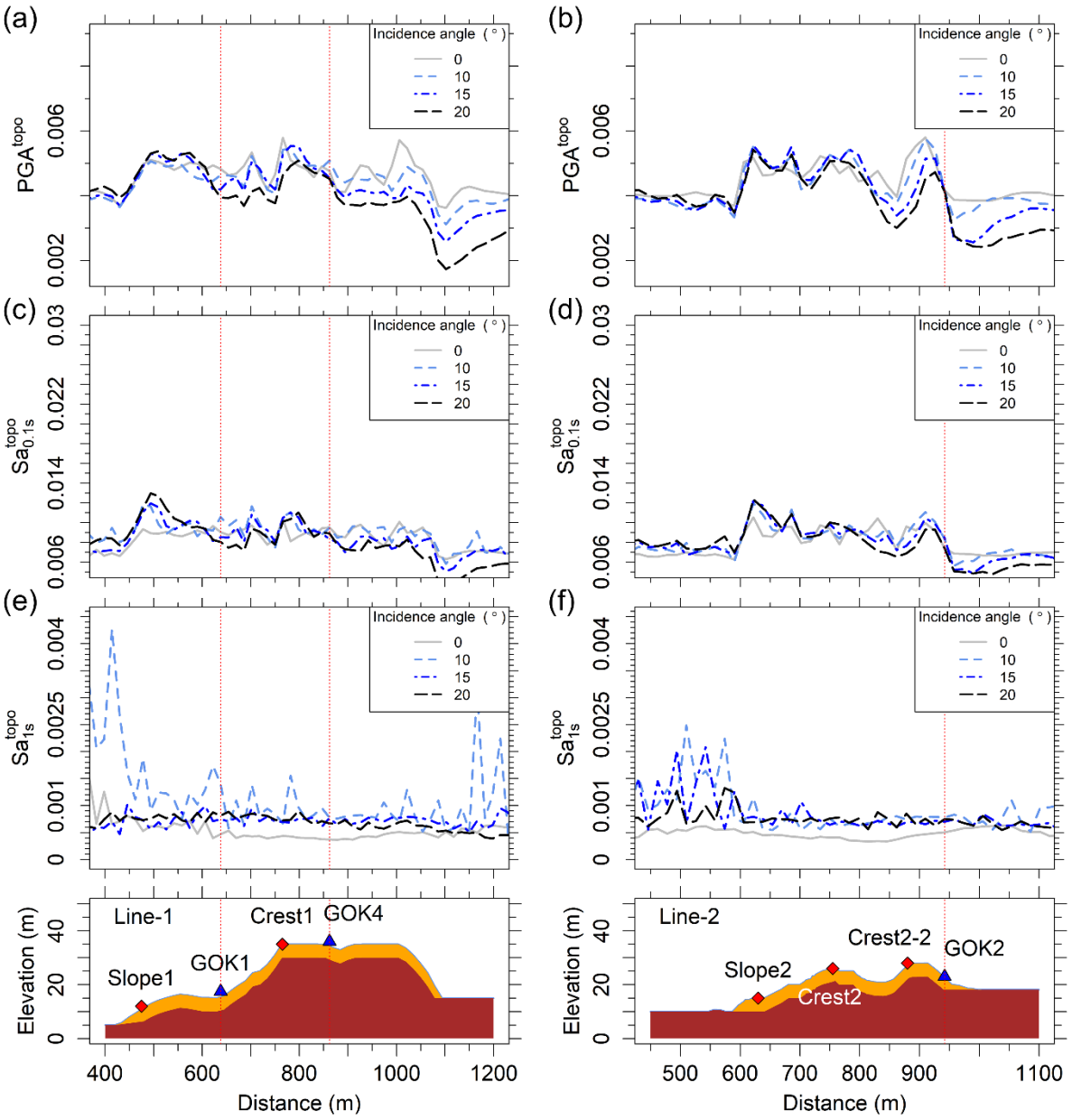

Figure 26. (a,b) PGA, (c,d) Sa at period of 0.1s, and (e,f) Sa at period of 1s of 2-layer model using Aftershock 2 as input wave in a horizontal direction on the ground surfaces of Line-1 and line-2 relative to the free-field, respectively, for four different incidence angles (0°, 10°, 15°, and 20°).

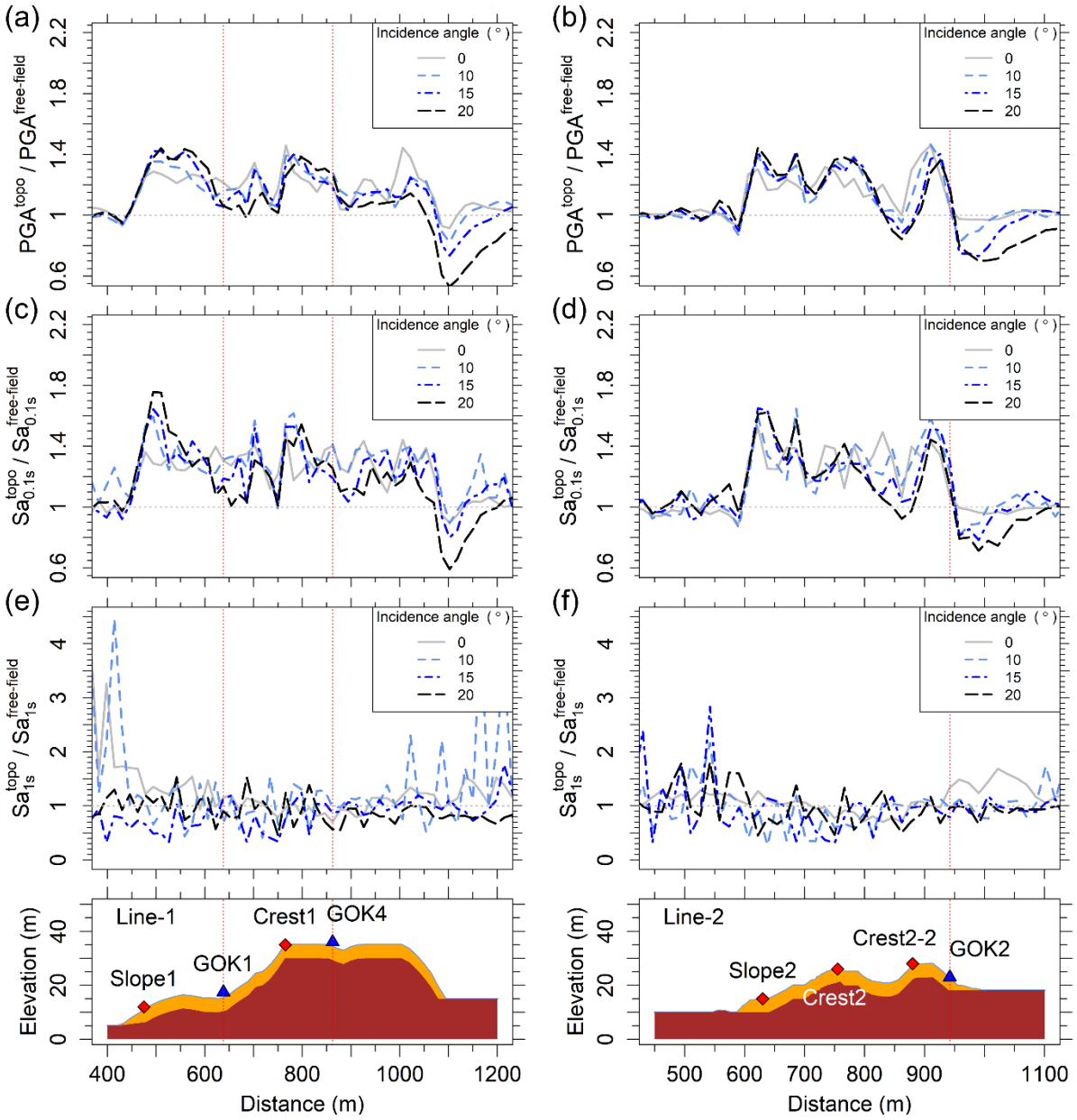

Figure 27. Amplification factors with respect to the free-field responses: (a,b) amplification factors of PGA (i.e., $PGA^{topo}/PGA^{free\text{-}field}$), (c,d) amplification factors of Sa at 0.1s (i.e., $Sa_{0.1s}{}^{topo}/Sa_{0.1s}{}^{free\text{-}field}$) , and (e,f) Sa at a period of 1s (i.e., $Sa_{1s}{}^{topo}/Sa_{1s}{}^{free\text{-}field}$) for the 2-layer models (Line-1 and Line-2, respectively) using the EW motion from Aftershock 2 as an input wave motion with four different incidence angles (0°, 10°, 15°, and 20°).

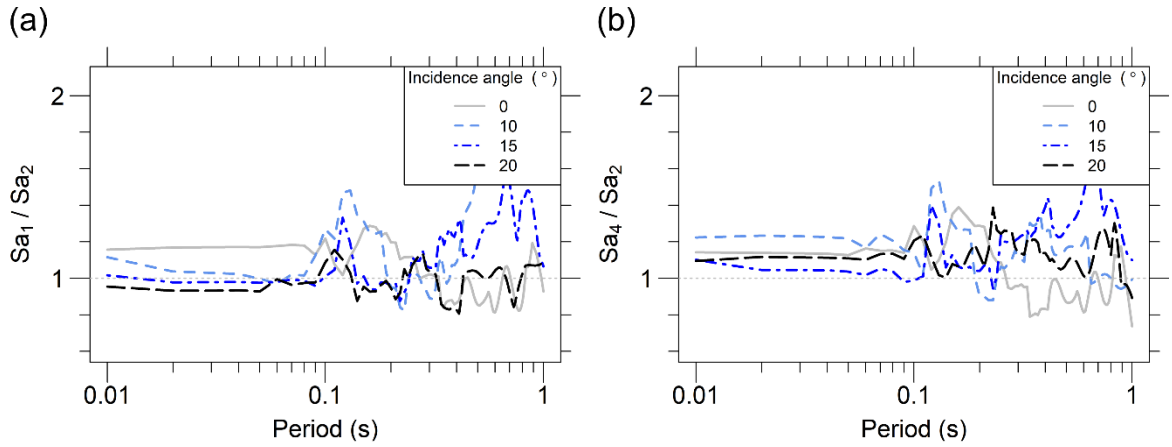

Figure 28. Ratio of the simulated Sas of 2-layer model using Aftershock 2 as input wave at GOK1 and GOK4 to those at GOK2 in a horizontal direction for four different incidence angles (0°, 10°, 15°, and 20°): (a) GOK1 to GOK2; (b) GOK4 to GOK2.

5.2. 4-layer model

Figure 29 shows the acceleration time series of the estimated ground motions for the 4-layer model using Aftershock 1 as input motion in a horizontal direction at GOK1, GOK2, and GOK4 for four different incidence angles: 0°, 10°, 15°, and 20°. The estimated ground motions match well with recorded ground motion. Figure 30 shows the 5% damped spectral acceleration of estimated ground motion corresponding to Figure 29. Similar with result of 2-layer model using Aftershock1 as input motion, PGAs at GOK1 and GOK4 are slightly larger than those at GOK2 and PGAs for 10° and 15° generally larger than those for other incidence angles.

Figure 31 shows PGA and Sa values at 0.1 s and 1 s estimated along Line-1 and Line-2 of 4-layer model. The PGA and Sa values are estimated to be larger on the slopes or plateaus facing the epicenter than those on the slope of opposite direction. The PGA and Sa values at crest of the slope are large with increasing incidence angle. The PGA and Sa values at GOK1 and GOK4 for 10° and 15° are generally larger than for other incidence angles. The value of PGA and Sa values at 0.1 s and 1 s are shown in Table 16, Table 17, and Table 18.

Figure 32 shows amplification factors which are defined as ratios of Sa values estimated at the topography models (Sa^{topo}) to those estimated at the free-field model ($Sa^{free\text{-}field}$) for three periods (i.e., PGA, 0.1 s and 1 s). The maximum amplifications of PGA (PGA^{topo} / $PGA^{free\text{-}field}$) range from approximately 1.38 to 1.66 at Crests and Slopes. The maximum amplifications of Sa at 0.1 s (Sa^{topo} / $Sa^{free\text{-}field}$ at period of 0.1s) range from approximately 1.38 to 2.19 at Crests and Slopes. It shows that the Sa values are larger at the crests of the slopes facing the epicenter than those at the slopes facing in the opposite direction. The amplifications of Sa at 1 s (Sa^{topo} / $Sa^{free\text{-}field}$ at period of 1s) generally fluctuate on the unity.

The amplification factors of PGA, Sa at periods of 0.1s and 1 s for the 4-layer model using Aftershock 1's EW record as an input motion was shown in Table 19, Table 20, and Table 21 respectively. The amplification factors for PGA at Slopes, Crests, GOK1 and GOK4 are generally larger than those at GOK2. At Slope1 and Slope2, the amplification factors of PGA and Sa at 0.1 s for incidence angle of 15°, and 20° are generally larger than those for 0° and 10°. At GOK1 and GOK4, the amplification factors for PGA and Sa at 0.1 s for 20° are smallest values of those for four different angles. At Crest2-2, the amplification factors of PGA and Sa at 0.1 s for incidence angle of 20° are generally smaller than those for 0°, 10°, and 15°. The differences between the maximum amplifications at the slope crest and the minimum amplifications on the opposite slope are larger for the incidence angles of 20° than for the other incidence angles.

Figure 33 shows the Sas estimated for GOK1 (Sa_1) and GOK4 (Sa_4) normalized by those estimated for GOK2 (Sa_2), respectively, with period ranging from 0.01 to 1s for four incidence angle. The ratios are generally greater than the unity especially when the incidence angles are 10° and 15°. At periods of 0.01 s – 0.04 s, the ratios are always greater than the unity for all angles, and those for incidence angles of 10 and 15 are generally larger than those for incidence angles of 0° and 20° for both (Sa_1/Sa_2 and Sa_4/Sa_2). In addition, the ratios for incidence angles of 10° and 15° show the greater increase of ratio than those for incidence angles of 0° and 20° at periods longer than 0.1 s.

Table 16. PGA for Estimated acceleration of 4-layer model using Aftershock 1 as input in a horizontal direction at a location of GOK1, GOK2, and GOK4 for four different incidence angles (0°, 10°, 15°, and 20°).

PGA (g)				
	0°	10°	15°	20°
GOK1	0.046	0.049	0.049	0.048
GOK2	0.045	0.044	0.044	0.044
GOK4	0.047	0.05	0.053	0.048
Slope1	0.048	0.058	0.065	0.068
Crest1	0.053	0.058	0.06	0.056
Slope2	0.053	0.061	0.067	0.07
Crest2	0.049	0.052	0.055	0.055
Crest2-2	0.052	0.055	0.056	0.051

Table 17. Sa at 0.1s for Estimated acceleration of 4-layer model using Aftershock 1 as input in a horizontal direction at a location of GOK1, GOK2, and GOK4 for four different incidence angles (0°,

10°, 15°, and 20°).

Sa at 0.1s (g)				
	0°	10°	15°	20°
GOK1	0.175	0.188	0.184	0.166
GOK2	0.171	0.174	0.185	0.191
GOK4	0.163	0.183	0.181	0.168
Slope1	0.186	0.232	0.254	0.296
Crest1	0.2	0.209	0.205	0.189
Slope2	0.207	0.259	0.276	0.298
Crest2	0.177	0.189	0.196	0.18
Crest2-2	0.174	0.188	0.187	0.197

Table 18. Sa at 1s for Estimated acceleration of 4-layer model using Aftershock 1 as input in a horizontal direction at a location of GOK1, GOK2, and GOK4 for four different incidence angles (0°, 10°, 15°, and 20°).

Sa at 1s (g)				
	0°	10°	15°	20°
GOK1	0.004	0.004	0.004	0.003
GOK2	0.003	0.003	0.003	0.003
GOK4	0.004	0.003	0.003	0.003
Slope1	0.004	0.004	0.003	0.003
Crest1	0.004	0.003	0.004	0.003
Slope2	0.003	0.004	0.004	0.003
Crest2	0.003	0.003	0.004	0.003
Crest2-2	0.003	0.003	0.003	0.003

Table 19. Amplification factor of PGA for Estimated acceleration of 4-layer model using Aftershock 1 as input in a horizontal direction at a location of GOK1, GOK2, and GOK4 for four different incidence angles (0°, 10°, 15°, and 20°).

.Amplification factor of PGA				
	0°	10°	15°	20°
GOK1	1.373	1.313	1.224	1.176
GOK2	1.332	1.214	1.217	1.23
GOK4	1.412	1.348	1.418	1.253

Slope1	1.445	1.493	1.553	1.525
Crest1	1.595	1.556	1.613	1.472
Slope2	1.587	1.628	1.663	1.64
Crest2	1.475	1.421	1.454	1.438
Crest2-2	1.546	1.507	1.559	1.382

Table 20. Amplification factor of Sa at 0.1s for Estimated acceleration of 4-layer model using Aftershock 1 as input in a horizontal direction at a location of GOK1, GOK2, and GOK4 for four different incidence angles (0°, 10°, 15°, and 20°).

Amplification factor of Sa at 0.1s				
	0°	10°	15°	20°
GOK1	1.621	1.491	1.448	1.196
GOK2	1.575	1.528	1.568	1.48
GOK4	1.502	1.556	1.469	1.285
Slope1	1.722	1.822	1.918	1.896
Crest1	1.843	1.773	1.555	1.431
Slope2	1.909	2.037	2.089	2.189
Crest2	1.64	1.587	1.51	1.38
Crest2-2	1.607	1.579	1.531	1.537

Table 21. Amplification factor of Sa at 1s PGA for Estimated acceleration of 4-layer model using Aftershock 1 as input in a horizontal direction at a location of GOK1, GOK2, and GOK4 for four different incidence angles (0°, 10°, 15°, and 20°).

Amplification factor of Sa at 1s				
	0°	10°	15°	20°
GOK1	1.154	1.113	0.726	1.095
GOK2	1.012	1.078	1.269	1.126
GOK4	1.183	1.044	1.103	0.888
Slope1	1.117	1.219	1.006	1.061
Crest1	1.392	1.145	1.427	1.489
Slope2	0.957	1.105	1.12	1.183
Crest2	1.08	1.168	1.44	1.629
Crest2-2	1.093	1.158	1.334	1.35

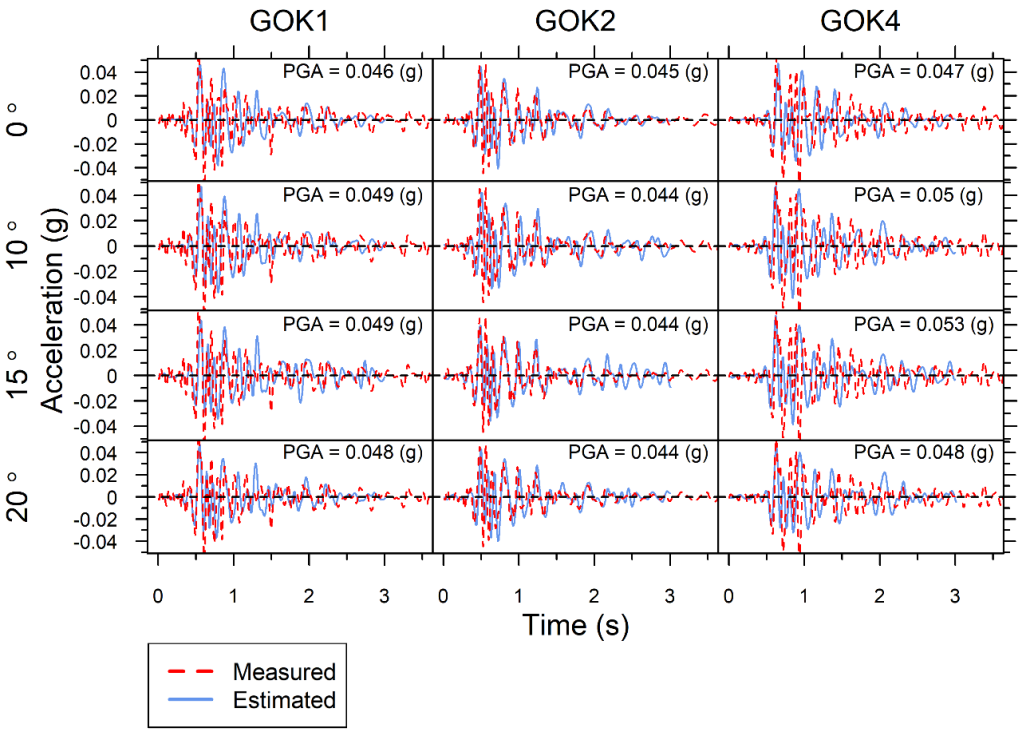

Figure 29. Estimated acceleration time series in a horizontal direction for the 4-layer model using Aftershock 1 as input wave at GOK1, GOK2, and GOK4 for four different incidence angles (0°, 10°, 15°, and 20°). The measured acceleration time series of Aftershock 1 in the EW direction are also presented.

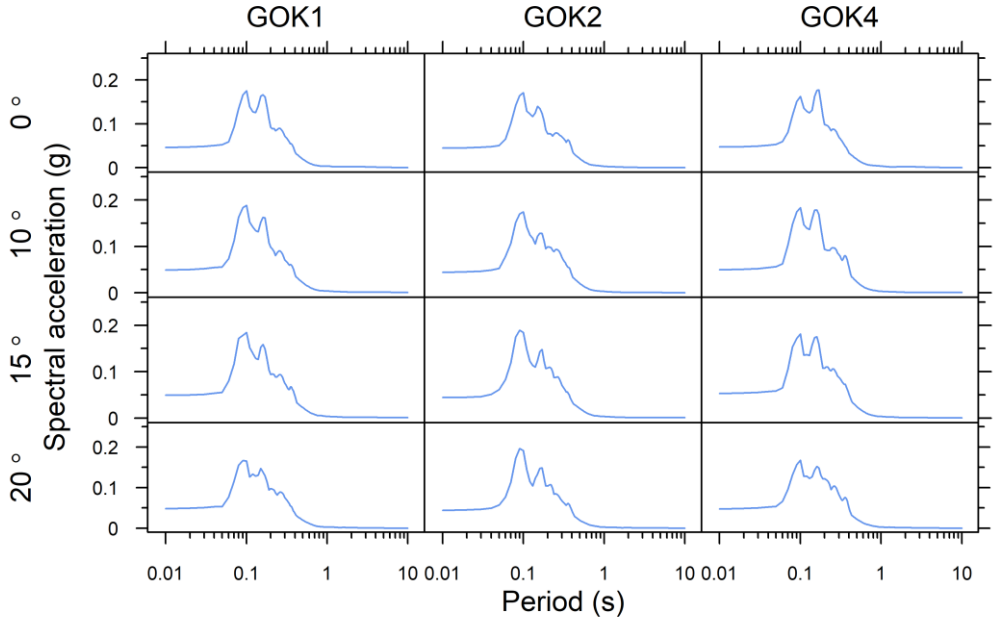

Figure 30. Estimated spectral acceleration in a horizontal direction for the 4-layer model using Aftershock 1 as input wave at GOK1, GOK2, and GOK4 for four different incidence angles.

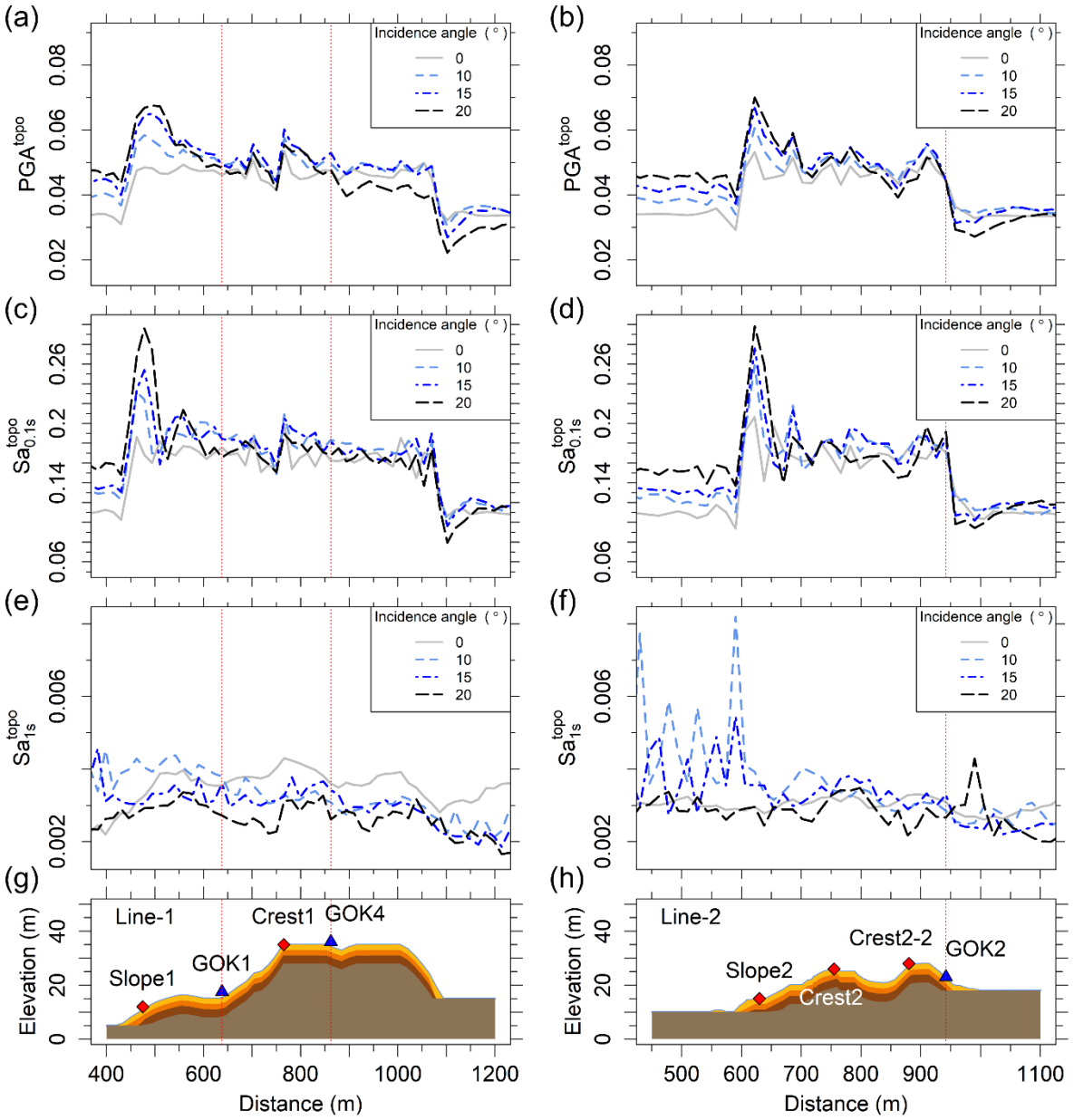

Figure 31. (a,b) PGA, (c,d) Sa at period of 0.1s, and (e,f) Sa at period of 1s of 4-layer model using Aftershock 1 as input wave in a horizontal direction on the ground surfaces of Line-1 and line-2 relative to the free-field, respectively, for four different incidence angles (0°, 10°, 15°, and 20°).

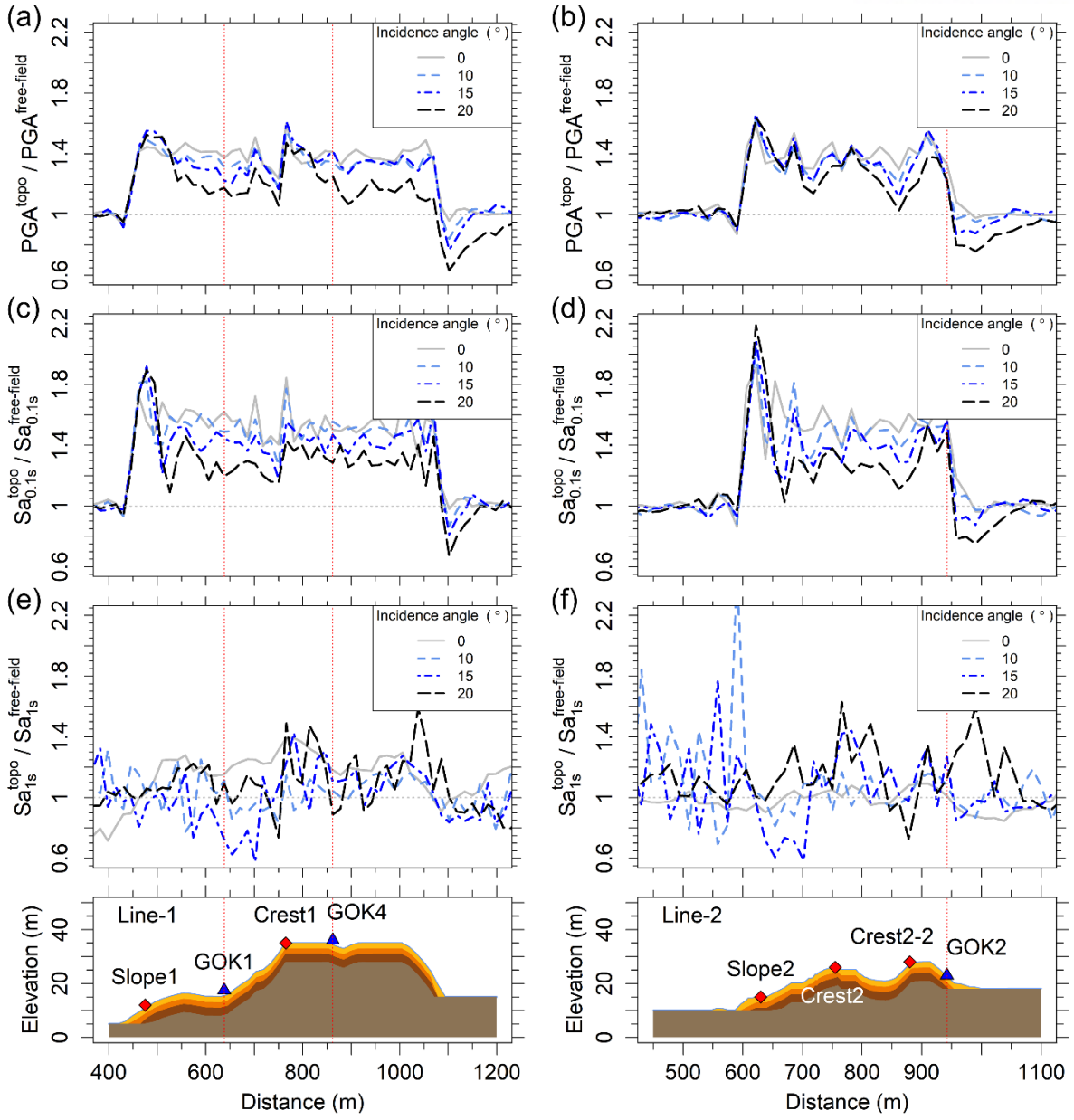

Figure 32. Amplification factors with respect to the free-field responses: (a,b) amplification factors of PGA (i.e., $PGA^{topo}/PGA^{free\text{-}field}$), (c,d) amplification factors of Sa at 0.1s (i.e., $Sa_{0.1s}{}^{topo}/Sa_{0.1s}{}^{free\text{-}field}$), and (e,f) Sa at a period of 1s (i.e., $Sa_{1s}{}^{topo}/Sa_{1s}{}^{free\text{-}field}$) for the 4-layer models (Line-1 and Line-2, respectively) using the EW motion from Aftershock 1 as an input wave motion with four different incidence angles (0°, 10°, 15°, and 20°).

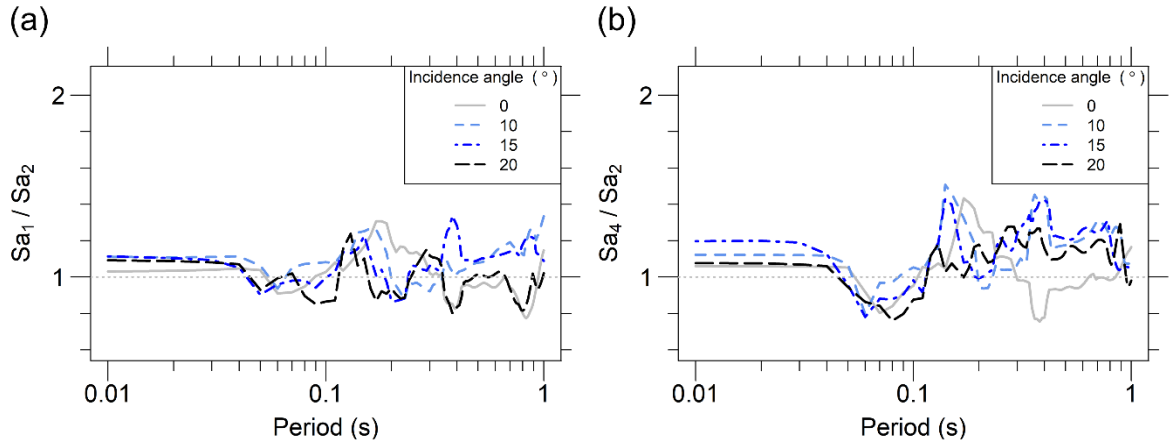

Figure 33. Ratio of the simulated Sas of 4-layer model using Aftershock 1 as input wave at GOK1 and GOK4 to those at GOK2 in a horizontal direction for four different incidence angles (0°, 10°, 15°, and 20°): (a) GOK1 to GOK2; (b) GOK4 to GOK2.

Figure 34 shows the acceleration time series of the estimated ground motions for the 4-layer model using Aftershock 2 as input motion in a horizontal direction at GOK1, GOK2, and GOK4 for four different incidence angles: 0°, 10°, 15°, and 20°. The estimated ground motions match well with recorded ground motion. Figure 35 shows the 5% damped spectral acceleration of estimated ground motion corresponding to Figure 34. Similar with result of 2-layer model using Aftershock 2 as input motion, PGAs at GOK1 and GOK4 are slightly larger than those at GOK2 . PGAs for 10° generally larger than those for other incidence angles.

Figure 36 shows PGA and Sa values at 0.1 s and 1 s estimated along Line-1 and Line-2 of 4-layer model. The PGA and Sa values are estimated to be larger on the slopes or plateaus facing the epicenter than those on the slope of opposite direction. The PGA and Sa values at crest of the slope are large with increasing incidence angle. The PGA and Sa values at GOK1 and GOK4 when the incidence angles are 0°, 10°, and 15° are generally larger than those when the incidence angle is 20°. The value of PGA and Sa values at 0.1 s and 1 s are shown in Table 22, Table 23, and Table 24.

Figure 37 shows the amplification factors which are defined as ratios of Sa values estimated at the topography models (Sa^{topo}) to those estimated at the free-field model ($Sa^{free\text{-}field}$) for three periods (i.e., PGA, 0.1 s and 1 s). The maximum amplifications of PGA (PGA^{topo} / $PGA^{free\text{-}field}$) range from approximately 1.38 to 1.54 at Crests and Slopes. The maximum amplifications of Sa at 0.1 s (Sa^{topo} / $Sa^{free\text{-}field}$ at period of 0.1s) range from approximately 1.33 to 1.93 at the Crests and Slopes. It shows that the Sa values are larger at the crests of the slopes facing the epicenter than those at the slopes facing in the opposite direction. The amplifications of Sa at 1 s (Sa^{topo} / $Sa^{free\text{-}field}$ at period of 1s) generally fluctuate on the unity however those on the Line-1 for 0° reach about 6.

The amplification factors of PGA, Sa at periods of 0.1s and 1 s for the 4-layer model using

Aftershock 2's EW record as an input motion was shown in Table 25, Table 26, and Table 27 respectively. The amplification factors for PGA at GOK1 and GOK4 are generally larger than those at GOK2. The amplification factors for Sa at 0.1s at GOK1 and GOK4 for 15° and 20° are larger than those at GOK2 however those at GOK1 and GOK4 for 0° and 10° are smaller than those at GOK2. The amplification factors of PGA and Sa at 0.1s at Slope1 and Slope2 for incidence angle of 15°, and 20° are generally larger than those for 0° and 10°. At Crest2-2, the amplification factors of PGA and Sa at 0.1 s for 20° are smallest values of those for four different angles. The differences between the maximum amplifications at the slope crest and the minimum amplifications on the opposite slope are large with increasing incidence angles.

Figure 38 shows the Sas estimated for GOK1 (Sa_1) and GOK4 (Sa_4) normalized by those estimated for GOK2 (Sa_2), respectively, with period ranging from 0.01 to 1s for four incidence angle. The ratios are generally greater than the unity. At periods of 0.01 s – 0.06 s, the ratios are always greater than the unity for all angles. In addition, the ratios for incidence angles of 0° and 10° show the greater increase of ratio than those for incidence angles of 15° and 20° at periods longer than 0.1 s.

Table 22. PGA for Estimated acceleration of 4-layer model using Aftershock 2 as input wave in a horizontal direction at a location of GOK1, GOK2, and GOK4 for four different incidence angles (0°, 10°, 15°, and 20°).

PGA (g)				
	0°	10°	15°	20°
GOK1	0.005	0.0047	0.0047	0.0041
GOK2	0.0042	0.0041	0.0041	0.0041
GOK4	0.0046	0.0055	0.005	0.0042
Slope1	0.0051	0.0052	0.0056	0.0058
Crest1	0.0056	0.0057	0.0057	0.0053
Slope2	0.005	0.0059	0.0062	0.006
Crest2	0.005	0.0056	0.0059	0.0052
Crest2-2	0.0055	0.0059	0.0054	0.0049

Table 23. Sa at 0.1s for Estimated acceleration of 4-layer model using Aftershock 2 as input wave in a horizontal direction at a location of GOK1, GOK2, and GOK4 for four different incidence angles (0°, 10°, 15°, and 20°).

Sa at 0.1s (g)				
	0°	10°	15°	20°
GOK1	0.0094	0.0105	0.0105	0.0075

GOK2	0.0074	0.0088	0.0094	0.0087
GOK4	0.0096	0.0106	0.0093	0.0084
Slope1	0.0091	0.0125	0.0132	0.0145
Crest1	0.0104	0.0116	0.0117	0.0114
Slope2	0.0101	0.0138	0.0149	0.015
Crest2	0.0093	0.0107	0.0104	0.0105
Crest2-2	0.0095	0.0112	0.0114	0.0101

Table 24. Sa at 1s for Estimated acceleration of 4-layer model using Aftershock 2 as input wave in a horizontal direction at a location of GOK1, GOK2, and GOK4 for four different incidence angles (0°, 10°, 15°, and 20°).

Sa at 1s (g)				
	0°	10°	15°	20°
GOK1	0.0022	0.0013	0.0012	0.001
GOK2	4.00E-04	0.001	0.0012	8.00E-04
GOK4	0.0012	0.0011	8.00E-04	0.001
Slope1	0.0014	0.0016	0.0011	0.001
Crest1	0.0018	0.001	0.0012	0.0015
Slope2	3.00E-04	0.0014	0.0012	0.0013
Crest2	4.00E-04	8.00E-04	0.0014	0.0012
Crest2-2	4.00E-04	0.0011	0.001	0.001

Table 25. Amplification factor of PGA for Estimated acceleration of 4-layer model using Aftershock 2 as input wave in a horizontal direction at a location of GOK1, GOK2, and GOK4 for four different incidence angles (0°, 10°, 15°, and 20°).

Amplification factor of PGA				
	0°	10°	15°	20°
GOK1	1.362	1.167	1.137	1.067
GOK2	1.148	1.033	1.107	1.129
GOK4	1.26	1.388	1.242	1.12
Slope1	1.394	1.368	1.431	1.442
Crest1	1.531	1.43	1.351	1.388
Slope2	1.387	1.489	1.51	1.536
Crest2	1.381	1.44	1.405	1.335

Crest2-2	1.496	1.472	1.439	1.333

Table 26. Amplification factor of Sa at 0.1s for Estimated acceleration of 4-layer model using Aftershock 2 as input wave in a horizontal direction at a location of GOK1, GOK2, and GOK4 for four different incidence angles (0°, 10°, 15°, and 20°).

Amplification factor of Sa at 0.1s				
	0°	10°	15°	20°
GOK1	1.511	1.474	1.204	1.029
GOK2	1.182	1.258	1.441	1.294
GOK4	1.543	1.568	1.289	1.147
Slope1	1.439	1.704	1.768	1.84
Crest1	1.668	1.616	1.508	1.576
Slope2	1.617	1.9	1.926	1.889
Crest2	1.509	1.543	1.334	1.332
Crest2-2	1.541	1.605	1.672	1.513

Table 27. Amplification factor of Sa at 1s PGA for Estimated acceleration of 4-layer model using Aftershock 2 as input in a horizontal direction at a location of GOK1, GOK2, and GOK4 for four different incidence angles (0°, 10°, 15°, and 20°).

Amplification factor of Sa at 1s				
	0°	10°	15°	20°
GOK1	5.621	1.593	0.496	1.103
GOK2	0.945	1.421	1.568	1.059
GOK4	3.267	1.313	1.006	0.851
Slope1	3.093	1.805	1.493	1.552
Crest1	4.797	1.496	1.334	2.07
Slope2	0.764	1.172	1.52	1.761
Crest2	0.926	1.151	1.232	1.976
Crest2-2	1.185	1.478	1.639	1.544

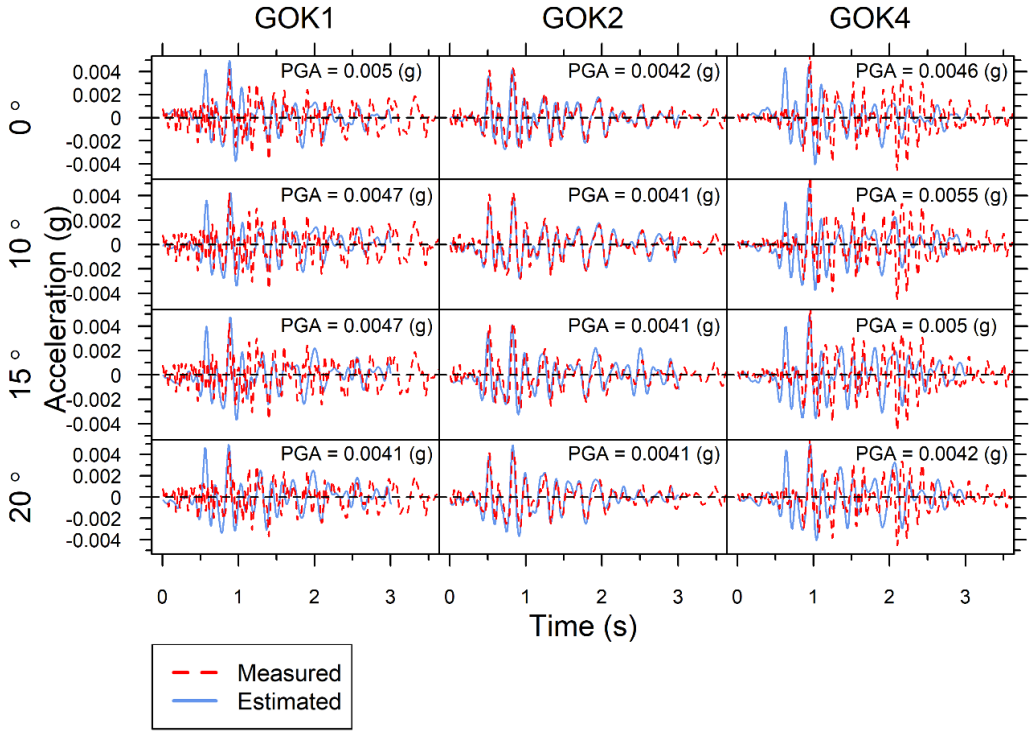

Figure 34. Estimated acceleration time series in a horizontal direction for the 4-layer model using Aftershock 2 as input wave at GOK1, GOK2, and GOK4 for four different incidence angles (0°, 10°, 15°, and 20°). The measured acceleration time series of Aftershock 2 in the EW direction are also presented.

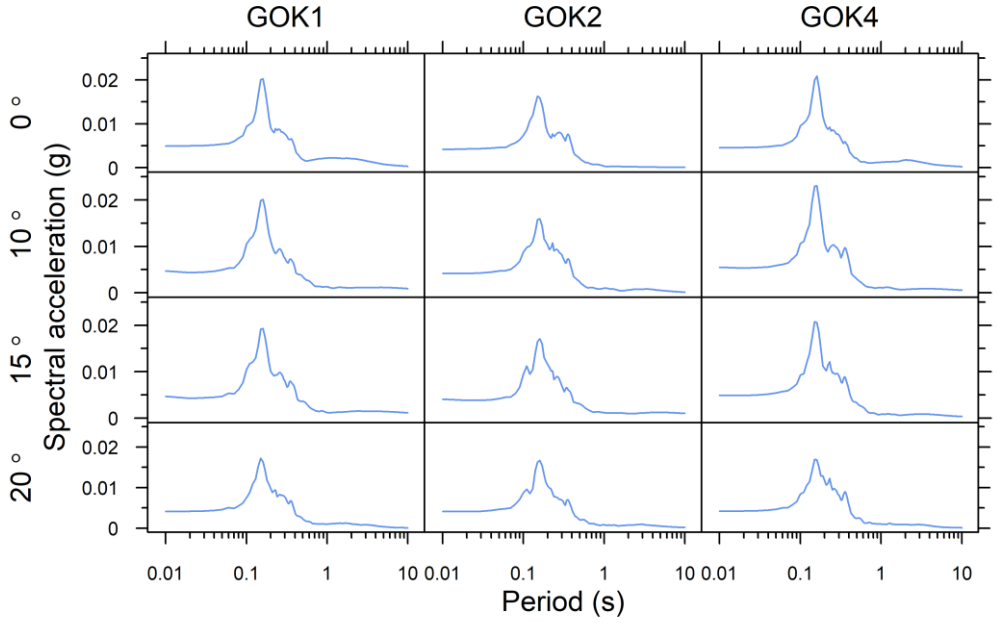

Figure 35. Estimated spectral acceleration in a horizontal direction for the 4-layer model using Aftershock 2 as input wave at GOK1, GOK2, and GOK4 for four different incidence angles.

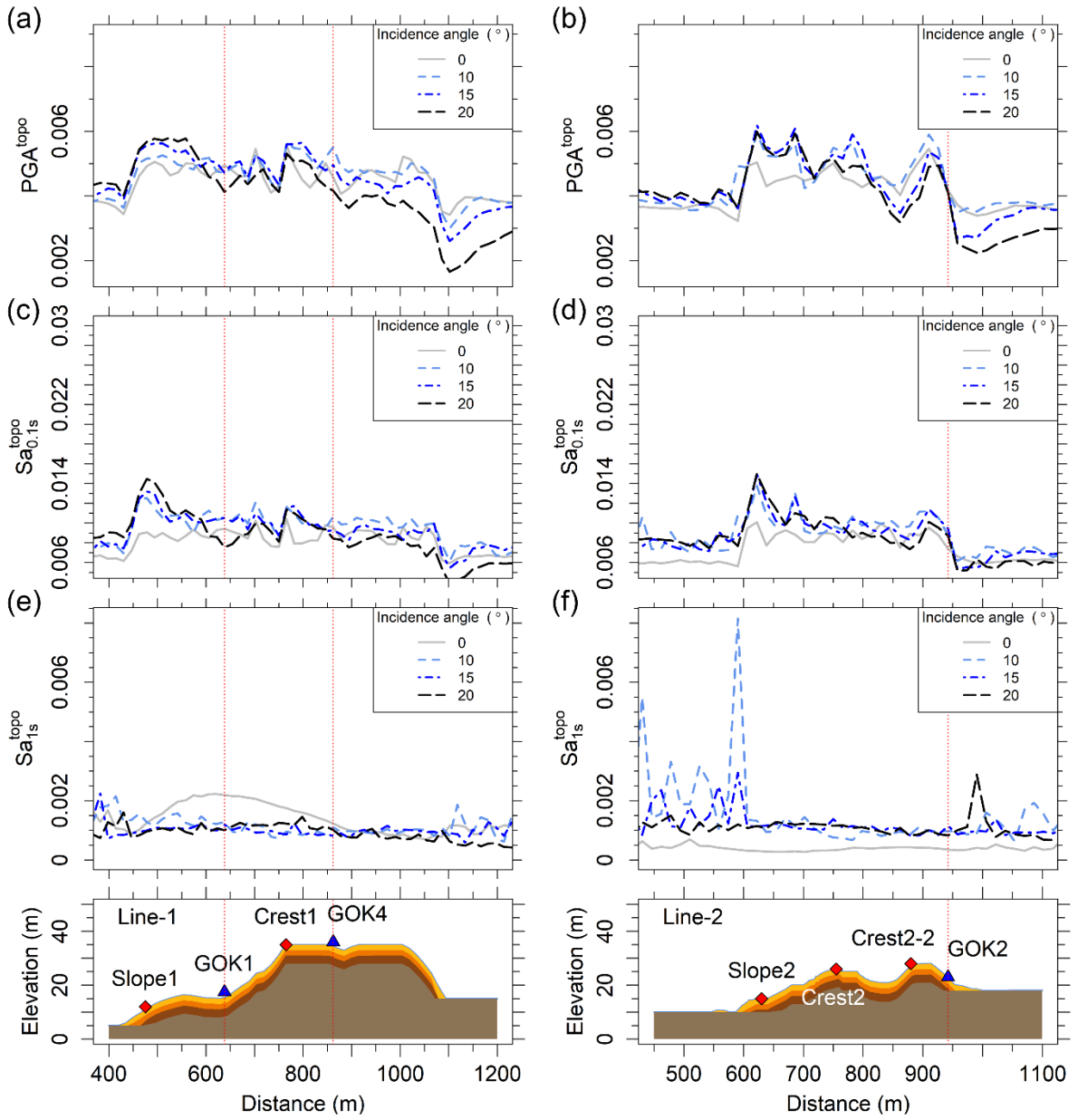

Figure 36. (a,b) PGA, (c,d) Sa at period of 0.1s, and (e,f) Sa at period of 1s of 4-layer model using Aftershock 2 as input wave in a horizontal direction on the ground surfaces of Line-1 and line-2 relative to the free-field, respectively, for four different incidence angles (0°, 10°, 15°, and 20°).

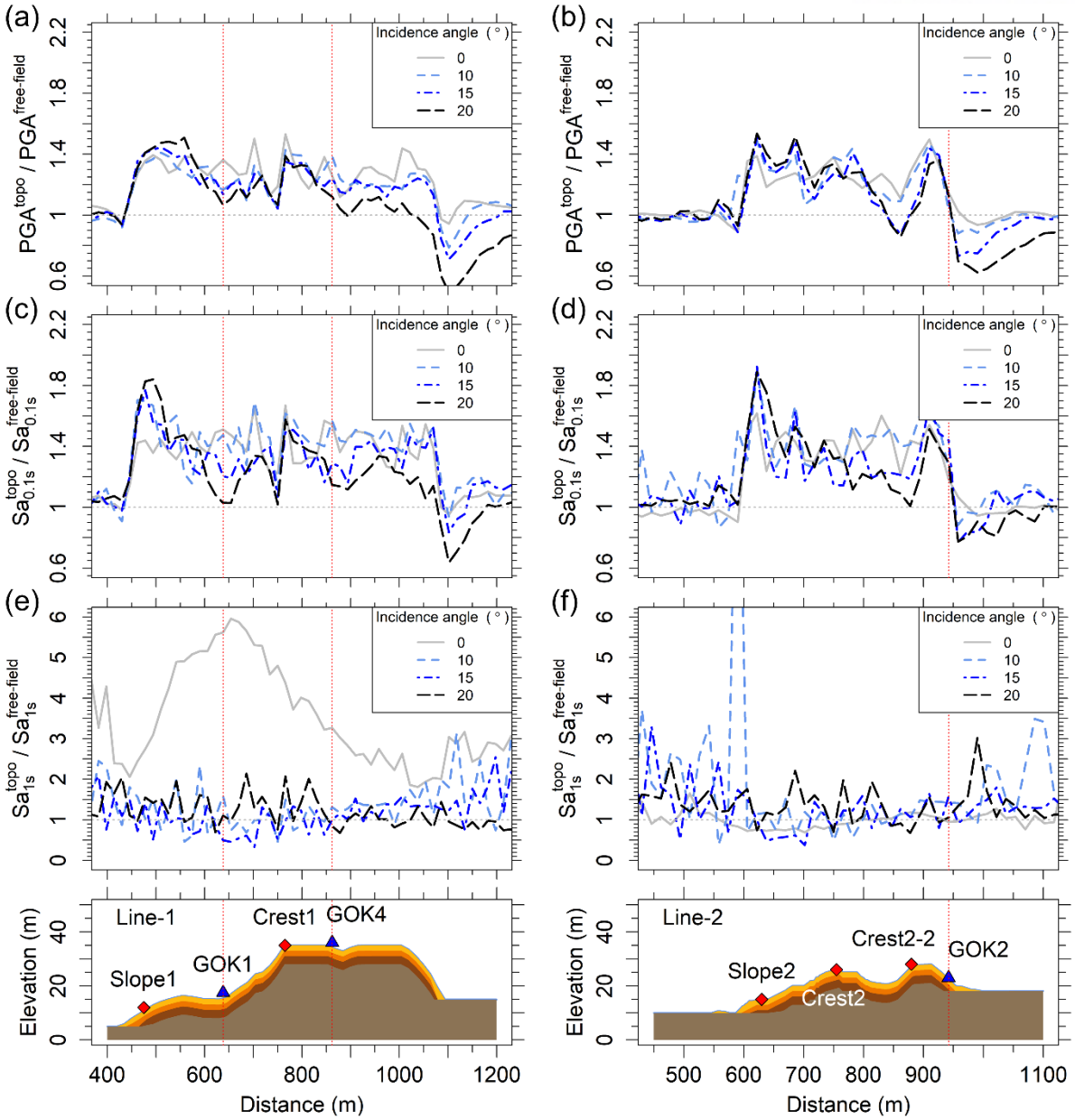

Figure 37. Amplification factors with respect to the free-field responses: (a,b) amplification factors of PGA (i.e., $PGA^{topo}/PGA^{free\text{-}field}$), (c,d) amplification factors of Sa at 0.1s (i.e., $Sa_{0.1s}{}^{topo}/Sa_{0.1s}{}^{free\text{-}field}$), and (e,f) Sa at a period of 1s (i.e., $Sa_{1s}{}^{topo}/Sa_{1s}{}^{free\text{-}field}$) for the 4-layer models (Line-1 and Line-2, respectively) using the EW motion from Aftershock 2 as an input wave motion with four different incidence angles (0°, 10°, 15°, and 20°).

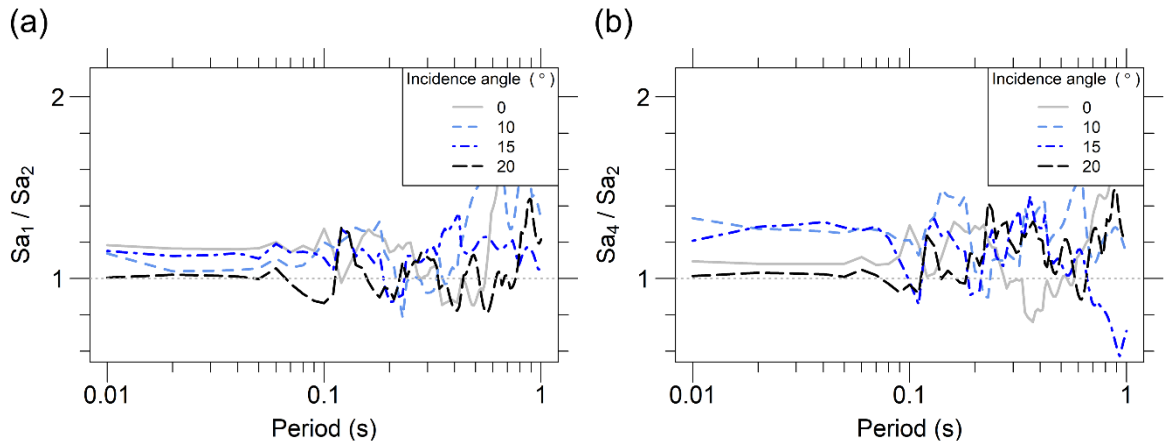

Figure 38. Ratio of the simulated Sas of 4-layer model using Aftershock 2 as input wave at GOK1 and GOK4 to those at GOK2 in a horizontal direction for four different incidence angles (0°, 10°, 15°, and 20°): (a) GOK1 to GOK2; (b) GOK4 to GOK2.

6. Discussion

Topographic effect is generally known to occur on the steep slope with a slope angle of 30° or higher. Despite that the slope angles in the study area were smaller than 10°, the ground motions were amplified by topographic effects, resulting in severe damage to houses located in certain areas. A series of numerical simulations revealed that ground motion amplifications occur at Slope1, the slope facing the epicenter. The ground motions estimated at the temporary stations of GOK1 and GOK4 were larger than those at the temporary station of GOK2. The amplifications occurred when the ground motions were reflected on the surface of the slope and concentrated at Slope1. In addition, surface waves can be generated by interaction between the ground surface and reflected P-waves, which might aggravate the ground motion amplifications.

In this study the max amplifications were generally located at Slope1 and Slope2. The amplification factors of PGA at Slope1 and Slope2 range approximately ~1.35 to 1.5 for incidence angles of 0°, 10°, 15°, and 20° and those of Sa at period of 0.1s range from ~1.54 to 1.88 for incidence angles of 0°, 10°, 15°, and 20°. When the 2-layer model used with AS 2 as an input motion, the amplification factors of PGA range from 1.29 to 1.42 for, and those of Sa at period of 0.1s range from 1.36 to 1.76.

In the case of 4-layer model using AS 1 as input motion, the amplification factors of PGA at Slope1 range from 1.44 to 1.66, and those of Sa at period of 0.1s range from 1.72 to 2.19. When the 4-layer model used with AS 2 as an input motion, the amplification factors of PGA at Slope1 range from 1.37 to 1.54, and those of Sa at period of 0.1s range from 1.44 to 1.93.

The amplification factors in frequency domain estimated by Ashford and Sitar (1997) at the ratio of slope height to wavelength of 1 (i.e. period of 0.1s) are approximately 1.5, 1.7, and 1.95 for incidence angle of 0°, 10°, and 20°, respectively. When Ashford and Sitar (1997) conducted analysis with three different input motion (i.e. ECNS, UCSC0 and JOS90), the amplification factors (i.e. amplification factors = a_{max}/a_{ffc}) for ECNS are 1.42, 1.54, and 1.74 for incidence angle of 0°, 10°, and 20°, respectively. Those for UCSC0 are 1.4, 1.56, and 1.89 for incidence angle of 0°, 10°, and 20°, respectively and those for JOS90 are 1.47, 1.57, and 1.94 for incidence angle of 0°, 10°, and 20°, respectively. The max amplifications near the crest estimated by Assimaki and Gazetas (2004) for incidence angle of 0° are different with domain profile and the values range from approximately 1.2 to 1.38. Our estimated amplification at Slope1 and Slope2 are similar with previous study.

amplification factors are dependent on incidence angle and number of layers. At the crest of a slope facing the epicenter, the amplification factors of simulated ground motions of 15° and 20° are generally larger than those of 0° and 10°. Furthermore, the amplification factors for the 4-layer model are generally larger than those of 2-layer model.

The ground motion amplifications were observed only for PGA and Sa at a period of 0.1s, but

not for Sa at a period of 1s. This was because the wavelengths of long period motions are longer than the slope dimension in the study area.

7. Conclusions

The Pohang, South Korea, earthquake occurred on November, 15, 2017. It caused severe damages to village which named Gokgang-ri which are consist of northern district and southern district near the epicenter and unusual damage pattern. The damage pattern showed that the northern district located on the slope facing the epicenter had serious damages, however, southern district located on the slope facing the opposite direction to the epicenter had only minor damages.

Two aftershocks (AS 1 and AS 2) recorded at temporary stations (GOK1, GOK2, and GOK4) were analyzed and it was found that ground motions recorded at GOK2 are generally smaller than those at GOK1 and GOK4.

Numerical simulations were conducted using the measured ground motions as input motions to investigate amplifications of ground motions. Topographic profiles of Gokgang-ri were described and two different models (2-layer model and 4-layer model) which have different number of layers, respectively and four different incidence angle (0°, 10°, 15°, and 20°) were simulated.

The amplification of estimated acceleration occurred at slope facing the epicenter. Accelerations in the horizontal direction estimated at the temporary stations of GOK1 and GOK4 were greater than those at GOK2. The amplifications for 15° and 20° were generally larger than those for 0° and 10°. The amplifications of 4-layer model were generally greater than those of 2-layer model.

Topographic effects can occur on gentle hill by incidence angle and number of layers using numerical simulation. In Korea, important buildings and infrastructures are often located on gentle hill. Therefore, it is important to understand the observation for ground motion predictions and the earthquake preparation.

REFERENCES

Ashford, S. A., & Sitar, N. (1997). Analysis of topographic amplification of inclined shear waves in a steep coastal bluff. *Bulletin of the Seismological Society of America, 87*(3), 692-700.

Assimaki, D., & Gazetas, G. (2004). Soil and topographic amplification on canyon banks and the 1999 Athens earthquake. *Journal of earthquake engineering, 8*(01), 1-43.

Assimaki, D., Kausel, E., & Gazetas, G. (2005). Soil-dependent topographic effects: a case study from the 1999 Athens earthquake. *Earthquake Spectra, 21*(4), 929-966.

Buech, F., Davies, T. R., & Pettinga, J. R. (2010). The Little Red Hill Seismic Experimental Study: Topographic Effects on Ground Motion at a Bedrock-Dominated Mountain Edifice. *Bulletin of the Seismological Society of America, 100*(5A), 2219-2229. doi:10.1785/0120090345

Davis, L. L., & West, L. R. (1973). Observed effects of topography on ground motion. *Bulletin*

of the Seismological Society of America, 63(1), 283-298.

Hong, T.-K., Lee, J., Kim, W., Hahm, I.-K., Woo, N. C., & Park, S. (2017). The 12 September 2016 ML5.8 midcrustal earthquake in the Korean Peninsula and its seismic implications. *Geophysical Research Letters, 44*(7), 3131-3138. doi:10.1002/2017gl072899

Itasca. (2011). FLAC – Fast Lagrangian Analysis of Continua. Retrieved from retrieved from https://www.itascacg.com

Kang, S., Kim, B., Bae, S., Lee, H., & Kim, M. (2019a). Earthquake-induced ground deformations in the low-seismicity region: A case of the 2017 M5. 4 Pohang, South Korea, earthquake. *Earthquake Spectra, 35*(3), 1235-1260.

Kang, S., Kim, B., Cho, H., Lee, J., Kim, K., Bae, S., & Sun, C. G. (2019b). Ground-Motion Amplifications in Small-Size Hills: Case Study of Gokgang-ri, South Korea, during the 2017 ML 5.4 Pohang Earthquake Sequence. *Bulletin of the Seismological Society of America, 109*(6), 2626-2643.

Kim, K.-H., Ree, J.-H., Kim, Y., Kim, S., Kang, S. Y., & Seo, W. (2018). Assessing whether the 2017 Mw 5.4 Pohang earthquake in South Korea was an induced event. *Science, 360*(6392), 1007-1009.

Korea Meteorological Administration. (2017). *Detailed analysis of 15 Nov Pohang earthquake*. Retrieved from http://www.kma.go.kr/notify/press/kma_list.jsp?bid=press&mode=view&num=1193456&page=3&field=&text=1

Korea Meteorological Administration. (2018). *Pohang earthquake analysis report*. Retrieved from https://www.weather.go.kr/weather/earthquake_volcano/earthquake_pohang.pdf

Lysmer, J., & Kuhlemeyer, R. L. (1969). Finite dynamic model for infinite media. *Journal of the Engineering Mechanics Division, 95*(4), 859-878.

National Emergency Management Agency. (2012). *Active Fault Map and Seismic Hazard Map*. (NEMA-2009-24).

Pedersen, H., Le Brun, B., Hatzfeld, D., Campillo, M., & Bard, P.-Y. (1994). Ground-motion amplitude across ridges. *Bulletin of the Seismological Society of America, 84*(6), 1786-1800.

Sepúlveda, S. A., Murphy, W., Jibson, R. W., & Petley, D. N. (2005). Seismically induced rock slope failures resulting from topographic amplification of strong ground motions: The case of Pacoima Canyon, California. *Engineering geology, 80*(3-4), 336-348.

Son, M., Kim, I.-S., & Sohn, Y. K. (2005). Evolution of the Miocene Waup Basin, SE Korea, in response to dextral shear along the southwestern margin of the East Sea (Sea of Japan). *Journal of Asian Earth Sciences, 25*(3), 529-544. doi:https://doi.org/10.1016/j.jseaes.2004.06.003

Stewart, J. P., & Sholtis, S. E. (2005). Case study of strong ground motion variations across cut slope. *Soil Dynamics and Earthquake Engineering, 25*(7), 539-545. doi:https://doi.org/10.1016/j.soildyn.2004.11.004